J. Fluid Mech. (1995), *vol.* 304, *pp.* 47–86

Compressible vortex reconnection

By D. VIRK[1], F. HUSSAIN[1] AND R. M. KERR[2]

[1]Department of Mechanical Engineering,
University of Houston, Houston, TX 77204-4792, USA
[2]Geophysical Turbulence Program, NCAR, Boulder, CO 80307-3000, USA

(Received 28 June 1994 and in revised form 19 July 1995)

Reconnection of two antiparallel vortex tubes is studied as a prototypical coherent structure interaction to quantify compressibility effects in vorticity dynamics. Direct numerical simulations of the Navier–Stokes equations for a perfect gas are carried out with initially polytropically related pressure and density fields. For an initial Reynolds number ($Re = \Gamma/\nu$, circulation divided by the kinematic viscosity) of 1000, the pointwise initial maximum Mach number (M) is varied from 0.5 to 1.45. At M=0.5, not surprisingly, the dynamics are essentially incompressible. As M increases, the transfer of Γ starts earlier. For the highest M, we find that shocklet formation between the two vortex tubes enhances early Γ transfer due to viscous cross-diffusion as well as baroclinic vorticity generation. The reconnection at later times occurs primarily due to viscous cross-diffusion for all M. However, with increasing M, the higher early Γ transfer reduces the vortices' curvature growth and hence the Γ transfer rate; i.e. for the Re case studied, the reconnection timescale increases with M. With increasing M, reduced vortex stretching by weaker 'bridges' decreases the peak vorticity at late times. Compressibility effects are significant in countering the stretching of the bridges even at late times. Our observations suggest significantly altered coherent structure dynamics in turbulent flows, when compressible.

1. Introduction

Turbulence is necessarily vortical, and the large-scale, coherent structures observed in turbulent shear flows are now well accepted as vortical entities. We believe that an understanding of vortex dynamics is crucial for applying the coherent structure concept to better understand and optimally control turbulence and associated phenomena (entrainment and mixing, heat and mass transports, combustion, drag and aerodynamic noise). Vortex dynamics may also provide an understanding of the physical mechanisms of large-scale/small-scale interaction, cascade and mixing (Melander & Hussain 1993).

Compressibility effects are significant in many technologically relevant flows. However, most of our knowledge of coherent structures and vortex dynamics – limited as it may be – is based on incompressible flows. Thus, two additional effects must be investigated: (i) baroclinic vorticity generation (also possible in stratified incompressible flows), and (ii) non-solenoidal velocity, which may produce shocks at sufficiently high Mach numbers (M). Both effects alter the vorticity field and hence vortex interactions. Further, recall that by Helmholtz decomposition of the instantaneous velocity field, we can formally obtain the rotational and solenoidal velocity ($\boldsymbol{u}^{I}$), and irrotational and non-solenoidal velocity ($\boldsymbol{u}^c$). Biot-Savart induction – the cornerstone of incompressible vortex dynamics – provides $\boldsymbol{u}^I$ for a given vorticity field, but in compressible flows the total velocity field also includes $\boldsymbol{u}^c$ associated with dilatation and compression.

Since direct numerical simulations (DNS) of the compressible Navier–Stokes equations and quantitative experimental measurements in practical (complex) turbulent flows, when possible, are not only expensive but also difficult to analyse in terms of essential physical mechanisms, studies of idealized configurations are first necessary. The present work shows how compressibility affects one vortex interaction – *vortex reconnection*. This interaction is selected because of its expected relevance to energy cascade, turbulent mixing, turbulence production, aeroacoustic noise and helicity generation (Hussain 1986); also, vortex reconnection is prominent during mixing layer transition (Moser & Rogers 1993; Schoppa, Hussain & Metcalfe 1995). A striking example of reconnection is the evolution of large-scale aircraft contrails (Crow 1970). This same process is expected to occur at all scales in turbulent flows, as supported by vortex filament simulations by Siggia (1985), where the initial filaments always evolved into a (antiparallel) configuration conducive to viscous reconnection. In fact, studies so far of reconnections in interacting vortical structures seem to involve a locally antiparallel configuration irrespective of initial orientations (see Kida & Takaoka 1987; Oshima & Izutzu 1988; Kida, Takaoka & Hussain 1991*a*; Boratav, Pelz & Zabusky 1992) – this in magnetic reconnection parlance is called X-type reconnection; O-type vortex reconnection, which does not involve locally antiparallel vortex lines, has also been identified in isolated vortex rings with swirl by Virk, Melander & Hussain (1994).

Vortex reconnection is a three-dimensional, viscous (necessary for incompressible flows), topology-altering interaction of two adjacent vortex tubes. The topology is altered at points where vortex lines from the adjacent, initially separate, vortices intersect (at critical points; see figure 1*a*), and the reconnected vortex lines are accumulated into bundles orthogonal to the initial vortices. If initially absent, critical points in vortex line topology cannot appear in inviscid incompressible flows, so reconnection is impossible without viscosity; yet it occurs on a convective rather than viscous timescale (Takaki & Hussain 1985; Schatzle 1987; Zabusky & Melander 1989). In the Kambe (1983) model of two opposite signed vorticity layers pressed together by a constant strain rate, vorticity annihilation occurs on a convective timescale; this model may be appropriate very early in the reconnection process.

Previous studies using experimental, theoretical and numerical approaches have considered only incompressible vortex reconnection. The results of each approach are briefly reviewed here.

Experimental studies Two reconnections are apparent in flow visualization studies of vortex ring collision (Fohl & Turner 1975; Schatzle 1987), and one reconnection has been observed in elliptic jets and elliptic rings (Hussain & Husain 1989). However, in an unsteady three-dimensional interaction, a scalar does not necessarily mark the evolutionary vortical structures. Frequently, markers are removed from regions of intense vortex stretching and accumulated in regions of vorticity compression. Thus, dynamically significant features of vortical interactions and evolution are frequently missed by flow visualization (Bridges, Husain & Hussain 1989). In fact, flow visualization did miss remnants of the initial vortices that were observed in DNS; such remnants ('threads') are crucial to cascade (discussed below). Quantitative data from the LDA study of vortex reconnection by Schatzle did not show the remnants, perhaps because successive reconnection events between two colliding rings had sufficient dispersion from event to event to smear the ensemble average. DNS by Kida *et al.* (1991*a*) conclusively reveals threads for various angles of collision of vortex rings.

Theoretical studies Takaki & Hussain (1985) constructed a highly idealized model based on symmetry and conservation of fluid impulse. This model is valid only near the interaction region since it uses polynomial expansions to express the local velocity field. Although this study was limited to symmetric interactions across the critical point, it was later seen that this restriction does not alter the essential dynamics (Melander & Hussain 1988, referred to here in as MH 1988; see also Melander & Hussain 1989, 1990). Since the interacting vortices as well as the reconnected vortices were constrained to lie in a plane, this model leads to 'recoil' vortex rings (not seen in simulations) to preserve impulse. The impulse in an actual flow is preserved by the self-induced velocity of the vortex tubes due to curvature. Thus, three-dimensionality is an essential feature of reconnection.

Saffman (1990) has proposed a phenomenological model, which relies on an axial pressure gradient within the interacting rectilinear vortex tubes to cause reconnection. However, the pressure gradient in the interaction region is likely to be also affected by the strong adjacent reconnected vortices. Also, the proposed phenomenology assumes that reconnected vortex lines lie in the same plane as the interacting vortices and fails to consider the most dominant aspect of vortex reconnection observed in DNS, namely 'bridges' (discussed below). Moreover, this model assumes that the strain rate is constant in the interaction region, contrary to the DNS result that the strain rate in the interaction region varies strongly in both space and time (MH 1988; Meiron *et al.* 1989; Kida *et al.* 1991*a*). Hence, comparisons of predictions of Saffman's model with DNS results (such as by Boratav *et al.* 1992 and Shelley, Meiron & Orszag 1993) show significant differences. The increase and eventual decay in the axial strain rate in the model, unlike its saturation in DNS (see Shelley *et al.*), is probably because the flow induced by the bridges is neglected. This bridge induction is a significant feature of the reconnection mechanism and may also cause the peak in vorticity to occur at earlier times as *Re* increases, as observed in DNS (Kerr & Hussain 1989). Saffman's model predicts peak vorticity at later times as *Re* increases; see Shelley *et al.* and Boratav *et al.* Clearly, realistic theoretical modelling of vortex reconnection is still lacking.

Numerical studies DNS has the advantage that it can provide details of the vorticity field and vortex line topology, which are not yet accessible through state-of-the-art measurement technology (see Meng & Hussain 1995). Indeed, DNS has provided a rich knowledge base for the physics of reconnection, albeit in idealized configurations. However, early simulations with complicated initial vorticity configurations (Kida & Takaoka 1987; Zabusky & Melander 1989) were difficult to interpret and, as a result, yielded little insight into the mechanism. Meiron *et al.*'s (1989) results were complicated by the sheath of negative vorticity surrounding the positive core in their self-annihilating 'zero circulation' vortices. Ashurst & Meiron (1987) considered the collision of two vortex rings and visualized only the first reconnection. Kida *et al.* (1989, 1991*a*) simulated the collision of two vortex rings and delineated the details of the two reconnections prominent in flow visualization by Fohl & Turner (1975).

MH (1988) used two antiparallel, sinusoidally perturbed vortex tubes as their initial condition, as shown in figure 1(*b*) (the perturbation was only to ensure sustained collision of the tubes), and analysed the intrinsic reconnection mechanism by first identifying three stages: inviscid advection, bridging, and threading. During *inviscid advection*, the vortices approach each other by self-induction, and their cores deform. Even though negligible circulation is transferred to the dividing plane (π_d; X,Z-plane in figure 1*b*) at this stage (i.e. essentially inviscid evolution), vortex filament simulations (such as by Siggia 1985) are not an adequate model of even the first phase because they ignore core deformation. This deformation will affect core dynamics

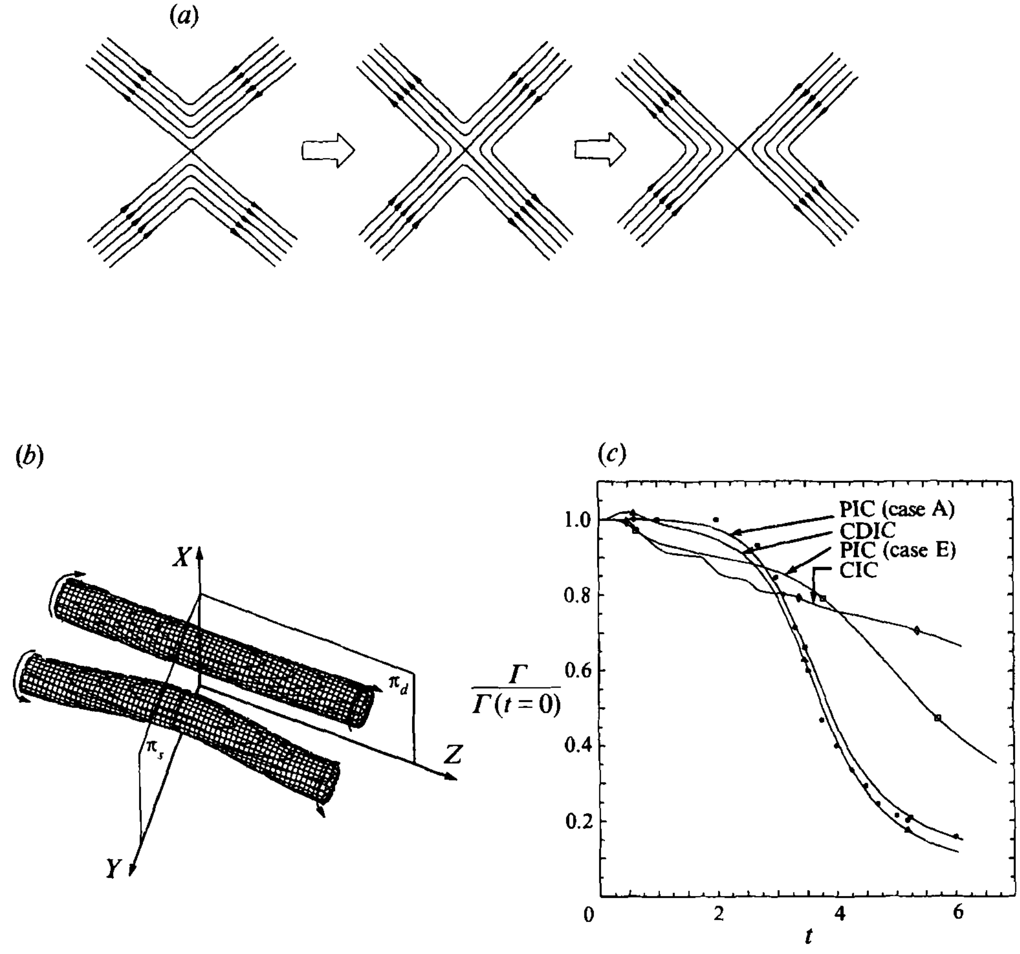

FIGURE 1 (*a–c*). For caption see facing page.

as well as local induction and hence is expected to significantly influence the rate of reconnection. In the crucial second stage, significant circulation is transferred from π_s (symmetric plane X, Y in figure 1*b*) to π_d, and *bridges* are formed as a result of a complex combination of three effects: mutual induction that increases vortex curvature and self-induction that sustains collision of the two initial vortices; vorticity stretching by parts of the vortex away from the interaction region; and viscous cross-diffusion which involves topological transformation equivalent to 'cut-and-connect' of vortex lines. The third stage, *threading*, occurs when the flow induced by bridges reverses the curvature of the initial vortices, thereby causing the vortices to move apart by self-induction, arresting the reconnection process. Thus, unreconnected remnants of the initial vortices remain as threads.

The existence of threads remains controversial, primarily because they have not been observed in flow visualization of vortex ring collision. However, their existence can be inferred from the elliptic jet data of Hussain & Husain (1989) and is clear in the flow visualizations of vortex rings near an inclined wall by Lim (1989). Threads are crucial for turbulence cascade since they may undergo a second curvature reversal leading to a second stage of smaller-scale reconnection and thus one should

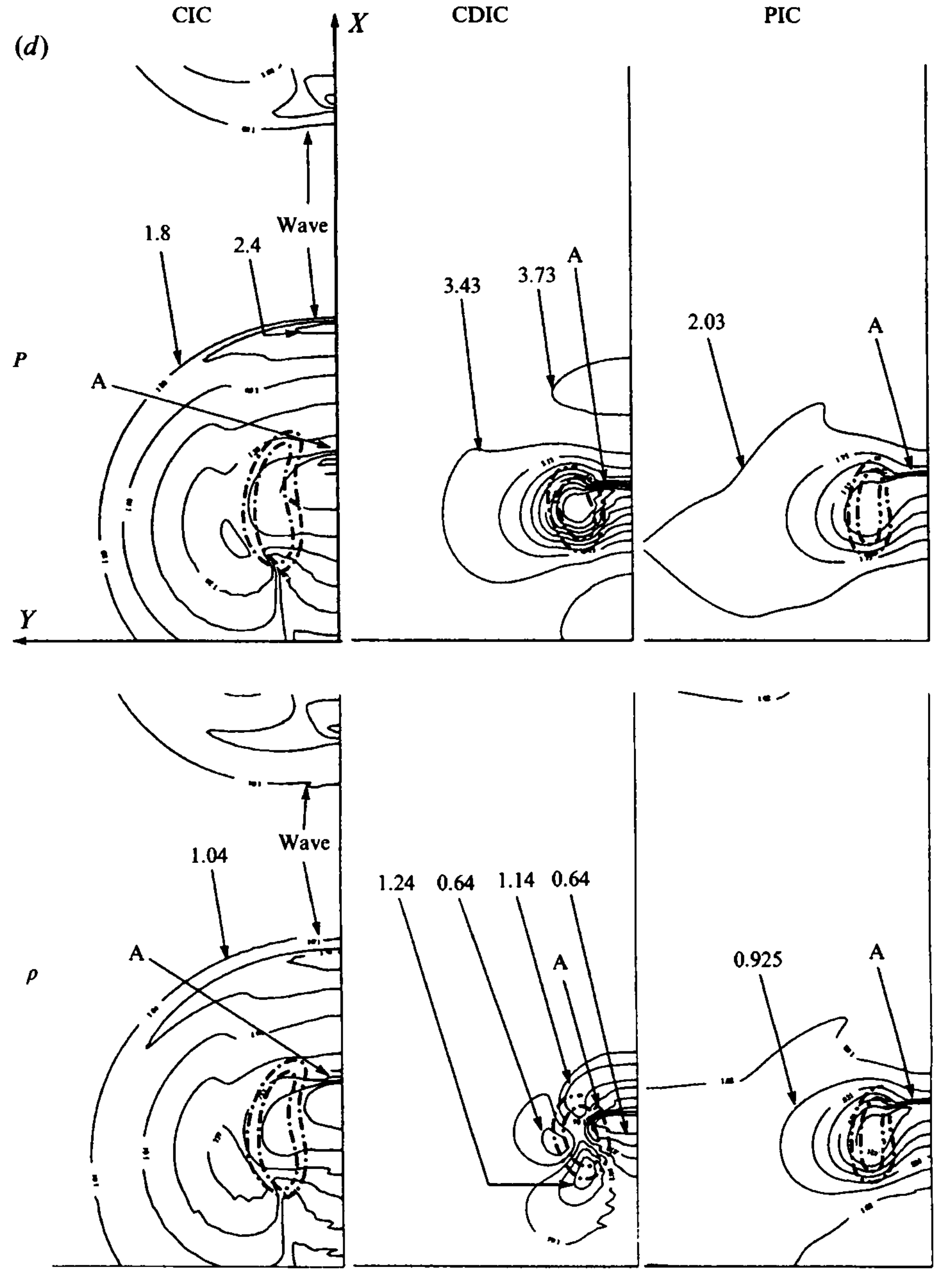

FIGURE 1. (*a*) Schematic of reconnection. (*b*) Initial vorticity distribution. Only the part of the vortices with positive X, Y and Z is actually computed. Plane X, Y is the symmetric plane π_s and the plane X, Z is dividing plane π_d. (*c*) The evolution of circulation in π_s for vortex reconnection simulations with different initial conditions. ○, PIC (case A, $M_{max}(t=0)=0.507$); ◇, CIC ($P=1.56$, $M_{max}(t=0)=1.442$); △, CDIC ($P=3.5$, $M_{max}(t=0)=1.500$); □, PIC (Case E, $M_{max}(t=0)=1.438$); ● are incompressible data from MH (1988). (*d*) The P and ρ fields in π_s with various initial conditions from (*c*). At $t=0.5$, the contour levels (minimum, maximum) with constant increment are: CIC P (0.24, 2.78), ρ (0.286, 1.52); CDIC P (0.75, 3.84), ρ (0.528, 1.257); PIC (case E) P (0.57, 2.29), ρ (0.34, 1.1). Chain-dotted lines are vorticity contours. A shocklet appears as large P and ρ gradients marked A.

expect subsequent reconnections (MH 1988). Successive reconnections appear to be a physical mechanism of cascade. Thus, in spite of some conflicting views (e.g. concerning existence of threads and location of bridging), DNS has provided considerable insight into incompressible vortex reconnection, and revealed bridging as the essential mechanism in the antiparallel configuration; similar details were also obtained by Kida *et al.* (1991*a*).

In the next section we briefly present the governing equations and the numerical method of solution. Section 3 contains a discussion of the initial conditions for vorticity, pressure (P) and density (ρ) fields. Differences in the evolution of low-M (essentially incompressible) and high-M reconnection are discussed in §4. The detailed mechanisms by which compressibility affects reconnection are discussed in §5; concluding remarks are presented in §6.

2. Equations and numerical method

We solve the compressible Navier–Stokes equations with specific volume $V(\equiv 1/\rho)$, velocity u_i, and pressure P as the primary variables. In non-dimensional form, the governing equations for mass, momentum, and energy are

$$\frac{\partial V}{\partial t} = -u_j \partial_j V + V(\partial_j u_j), \tag{1}$$

$$\frac{\partial u_i}{\partial t} = (\boldsymbol{u} \times \boldsymbol{\omega})_i - \partial_i(\tfrac{1}{2} u_j u_j) - \frac{1}{\gamma {M_o}^2} V \partial_i P + \frac{V}{Re_o} \partial_j (2\mu (D_{ij} - \tfrac{1}{3}\delta_{ij} D_{mm})), \tag{2}$$

$$\begin{aligned}\frac{\partial P}{\partial t} = {} & -(u_j \partial_j) P - \gamma P (\partial_j u_j) \\ & + \frac{\gamma(\gamma-1)}{Re_o} {M_o}^2 \mu (2 D_{ij} \partial_i u_j - \tfrac{2}{3} (\partial_j u_j)^2) + \frac{\gamma}{Pr Re_o} \partial_j (\kappa \partial_j (PV)).\end{aligned} \tag{3}$$

The fluid is assumed to be a perfect gas, i.e. $P^* = RT^*/V^*$ with zero bulk viscosity. In (1)–(3), $D_{ij} \equiv \frac{1}{2}(\partial_j u_i + \partial_i u_j)$, $\mathrm{V} \equiv V^*/V_o$, $u_i \equiv u_i^*/U_o$ and $\mathrm{P} \equiv P^* \gamma V_o / {c_o}^2$, where c_o is the reference sound speed and $\gamma \equiv C_p/C_v$ is the ratio of specific heats. The quantities with superscript $*$ are dimensional. Using scales $V_o = c_o = U_o = L = 1$ for corresponding quantities and κ_o and μ_o as fluid properties far away from the vortex core, we get the non-dimensional parameters: Prandtl number $Pr \equiv \mu_0 C_p/\kappa_0$, Reynolds number $Re_o \equiv U_o L / V_o \mu_0$, and Mach number $M_o \equiv U_o/c_o = 1$. Thus, in a simulation, local $M = M_o |\boldsymbol{u}| / (PV)^{1/2}$ and we define $Re \equiv \Gamma/(\mu_o V_o)$, where Γ is the circulation in π_s (see figure 1).

In the pseudo-spectral simulation code employed here, viscosity $\mu \equiv \mu^*/\mu_0$ and thermal conductivity $\kappa \equiv \kappa^*/\kappa_0$ may be prescribed functions of temperature ($T \equiv T^*/T_o$); however, for most of the simulations reported here we assume temperature-independent properties. This assumption significantly reduces the computation time and is justified in §5.4. Appropriate transforms accounting for boundary conditions are used to compute derivatives of the primary variables in wavenumber space and calculate the nonlinear terms in physical space. Because of the symmetries inherent in the initial conditions (figure 1*b*), only one half of a vortex is actually simulated. Thus, we use Fourier series in X for all variables, and cosine transforms in Y and Z for V, P and velocity u_1 along X. For u_2, the velocity along Y, we use sine transform in Y and cosine transform in Z; for u_3, we use cosine transform in Y and sine in Z. For timestepping, Wray's compact storage explicit scheme for the third-order Runge–

Kutta method is used (Wray 1987). The Courant number ($(u+c)_{max}\Delta t/\Delta x$, where u is fluid velocity and c is local sound speed) was 0.45 for all simulations reported here.

The choice of V, $\boldsymbol{u}$ and P as primary variables is motivated by the fact that it leads to only quadratic nonlinearities in the governing equations, whose aliasing errors can be removed by the 2/3 truncation procedure. Moreover, unlike formulations in terms of conservative variables (e.g. Feiereisen, Reynolds & Ferziger 1981), this choice of primary variables does not require any special splitting of the advection term in the momentum balance equation to maintain energy conservation. The energy variation (ΔE) over an entire simulation (approximately 12 turnover times for a fluid particle at the boundary of the initial compact vortex tube) was $\Delta E/E = 10^{-7}$, where $E = \rho u_i u_i/2 + P/(\gamma(\gamma-1)M_o^2)$ is the total energy.

To validate the code, we simulated the formation and propagation of a shock from a localized high pressure region as in Passot & Pouquet (1987). In these simulations, a fourth-order polynomial and at least ten grid points were necessary to approximate the initial pressure jump to suppress Gibbs phenomenon and obtain results within 1% of analytical predictions. We have also reproduced the two-dimensional compressible homogeneous turbulence results reported by Lee, Lele & Moin (1991) (see Virk & Hussain 1993; Virk 1993). In addition, excellent agreement was found between our low-M simulations and the incompressible vortex reconnection results reported by MH (1988) and obtained via an independently written code, as shown in §4.

3. Initial velocity field

The antiparallel configuration used by MH (1988) is selected for the present study because it does not involve the complicated 'fingering' phenomenon observed by Boratav *et al.* (1992); we feel that this fingering masked the essential physics in the simulations of Kida & Takaoka (1987) and Zabusky & Melander (1989). Fingering might occur in vortices before reconnection in a turbulent flow, but is not an essential aspect of the reconnection mechanism (Boratav *et al.*).

3.1. *Initial velocity field*

The initial vorticity distribution in the core was compact Gaussian as used in MH (1988):

$$\omega(\boldsymbol{x}) = \omega(r)(-a_v \sin(\alpha)\sin(Z)\hat{\boldsymbol{x}} + a_v \cos(\alpha)\sin(Z)\hat{\boldsymbol{y}} + \hat{\boldsymbol{z}}), \tag{4}$$

where
$$\omega(r) = \begin{cases} 10[1 - f(r/0.65)], & r < 0.65 \\ 0, & r \geqslant 0.65, \end{cases}$$

$$r^2 = (X - X_c - a_v \sin(\alpha)\cos(Z))^2 + (Y - Y_c + a_v \cos(\alpha)\cos(Z))^2$$

and
$$f(\eta) = \exp[-K\eta^{-1}\exp(1/(\eta-1))], \qquad K = \tfrac{1}{2}\exp(2)\log(2),$$

with $X_c + a_v \sin(\alpha)$ and $Y_c - a_v \cos(\alpha)$ being the centre of the vortex in the $Z = 0$ plane (see figure 1*b*). The vorticity profile is compact only initially since viscosity ensures non-zero vorticity outside the initial compact vorticity region at any $t > 0$. We choose a perturbation amplitude $a_v = 0.2$ and inclination angle $\alpha = 60°$ (the angle of the vortex axis, projected on the X, Y-plane, with the Y-axis). Initially in π_s, there is no gap between the two cores (i.e. vorticity-containing regions). Several low resolution runs showed that the sole effect of initially having a gap between the vortices, as in MH (1988), is a slight delay in the collision of two vortices, and hence in initiation of the circulation transfer, with no change in the essential dynamics. The sinusoidal perturbation in the initial state is only to ensure collision of the two antiparallel vortices to initiate reconnection and does not influence the essential local physics of the phenomenon. Using the above solenoidal vorticity field, we obtain the initial velocity field from the vector identity for a solenoidal velocity field,

$$\nabla^2 \boldsymbol{u} = -\nabla \times \boldsymbol{\omega}. \tag{5}$$

Since there is no consistent way to specify *a priori* the velocity divergence field, a solenoidal velocity field is initialized.

3.2. *Initial pressure and specific volume fields*

The initial polytropically related P and V fields were determined from the equations

$$P = aV^{-b}, \qquad \nabla \cdot (V \nabla P) = -\gamma M_o{}^2 \nabla \cdot (\boldsymbol{u} \cdot \nabla \boldsymbol{u}). \tag{6a, b}$$

Equation (6*b*) is obtained by imposing, for an inviscid flow, zero dilatation rate ($\partial(\nabla \cdot \boldsymbol{u})/\partial t = 0$) in the initially incompressible field. After substituting (6*a*) in (6*b*), the resulting Poisson equation for V is solved directly; we call this the polytropic initial condition (PIC; Virk & Hussain 1993). For the present simulations, we used $b = \gamma$, which leads to an initially homentropic flow field. The constant a determines ambient pressure, hence the speed of sound, and was used to vary M. The PIC was chosen after comparison with two other initial conditions: (i) constant P and V (constant initial condition CIC), and (ii) P determined from (6*b*) by imposing zero rate of change of divergence for constant V (constant density initial condition CDIC). CIC was used by Lee *et al.* (1991), and CDIC was used by Feiereisen *et al.* (1981) for compressible turbulence simulations. Vortex reconnection dynamics with CDIC were nearly incompressible even at high M, and strong initial transients were observed with CIC (Virk & Hussain). This is clearly illustrated by the evolution of Γ_s (circulation in π_s) for the three initial conditions (figure 1*c*). Simulation with CDIC shows some generation of Γ_s (due to baroclinic effects) at early time, but for $t > 1$ the evolution, despite high M, is surprisingly similar to that in the incompressible case (MH 1988). With CIC, note the drops in Γ_s around t=1.8, 2.5 and 3.5. These are due to wave–vortex interactions, where a pressure wave is created by the initially unbalanced centrifugal force in the vortex; see figure 1(*d*) where the wave is clear in the contours of P and ρ. Owing to periodic boundary conditions, this wave interacts with the vortices at later times. In contrast, simulation with PIC shows no such sudden Γ_s changes since the centrifugal force in the vortex is initially balanced by the radial pressure gradient. We obtain 'clean' simulations with PIC which shows compressibility effects not observed with CDIC. Additionally, based on entropy considerations, experimental observations of an almost polytropic relation between P and V in compressible vortices (Howard & Matthews 1956; Mandella 1987), and analysis using low-M asymptotic theories of the compressible Navier–Stokes equations by Erlebacher *et al.* (1990) and Zank & Matthaeus (1991), PIC appears more appropriate to study compressible vortex dynamics (see Virk & Hussain 1993).

In table 1, the parameters for the simulations reported in this paper are listed along with the letters used for identification in the discussion. We use the same non-dimensionalization for time as in MH (1988), i.e. $t = t^{*}\omega(t^{*} = 0)/20$, in order to allow direct comparison with their incompressible simulation.

Case	$M_{max}(t=0)$	$P = aV^{-b}$	Remarks
A	0.50	$13V^{-1.4}$	$Re = 1000$
B	0.95	$4V^{-1.4}$	$Re = 1000$
C	1.14	$2.9V^{-1.4}$	$Re = 1000$
D	1.28	$2.4V^{-1.4}$	$Re = 1000$
E	1.45	$2V^{-1.4}$	$Re = 1000$
F	1.45	$2V^{-1.4}$	$Re = 1000,\ \mu/\mu_o = (T/T_o)^{0.76}$
G	1.45	$2V^{-1.4}$	$Re = 1500$

TABLE 1. Initial conditions. V_o=1.0, and $Pr = 0.67$ for all simulations. Domain was $(9.86\times4.8\times4.8)r_v$, where r_v is core radius. Resolution was 128 × 65 × 65, except for case G which had resolution 256 × 65 × 65. The evolution of cases C and E was also calculated up to $t = 3$ with resolution 512 × 65 × 65; except for suppression of the Gibbs phenomenon when the shocklet occurs, the dynamics remained the same. For all cases $a_v = 0.2$, $Y_c = r_v + 0.1$.

4. Observations

4.1. *Vorticity isosurfaces*

The $|\omega|$ isosurfaces for cases A ($M = 0.5$) and E ($M = 1.45$) are shown in figure 2. Note that these vorticity surfaces are quite different from vortex surfaces because vortex lines can cross the former. Nevertheless, vorticity isosurfaces adequately mimic the topology of vortex surfaces in this simple configuration and are much easier to compute (also see §5.3). The $|\omega|$ isosurfaces in these two cases at early times are similar to the incompressible case (MH 1988). For case A, the entire evolution is virtually identical to that observed for incompressible vortex reconnection (MH 1988). In particular, note the strong bridges already clear at $t = 4.1$. In addition, the threads are clear at $t = 6.0$ and have undergone curvature reversal as for incompressible evolution (MH 1988). At high M, the bridges are weak even at $t = 4.5$. The threads are much stronger at $t = 6.0$, having no curvature reversal. The circulations in π_s and π_d for case E at $t = 6.0$ are the same as in case A at $t = 4.1$. However, the corresponding structure of the vortices is very different for the two cases. Namely, the bridges are farther apart (see §5.2) in case E than in case A, and the axes of interacting vortices lie in an X =constant plane in case E, in contrast to the elevated interaction region (relative to vortex legs) for case A. These observations suggest that compressibility effects delay and suppress reconnection.

4.2. *Vorticity in π_s and π_d cross-sections*

To illustrate the vorticity evolution in the interaction region, we show the time evolution of vorticity contours in π_s and π_d in figures 3 and 4(*a*) respectively, for cases A and E. In figure 3, note that even though vorticity contours are only slightly deformed in the 'inviscid advection' stage ($t < 2.0$) for low M, those for high M are tilted towards π_d in front of the vortex dipole formed in π_s. This is due to the formation of a shocklet (see §5). At times $t = 3.6$ and 4.5, it is clear that the characteristic head–tail structure in π_s observed by MH (1988) and Kida *et al.* (1991*a*) occurs in case A, but not in case E. Since the deformation of a vortex dipole into a head–tail structure is strongly dependent on the straining flow in the dipole plane (Buntine & Pullin 1987; Kida, Takaoka & Hussain 1991*b*), this indicates that such a straining flow is reduced as M increases; the reduction in strain rate is a result of slower growth of the sinusoidal perturbation (see §5). Finally, we note that the

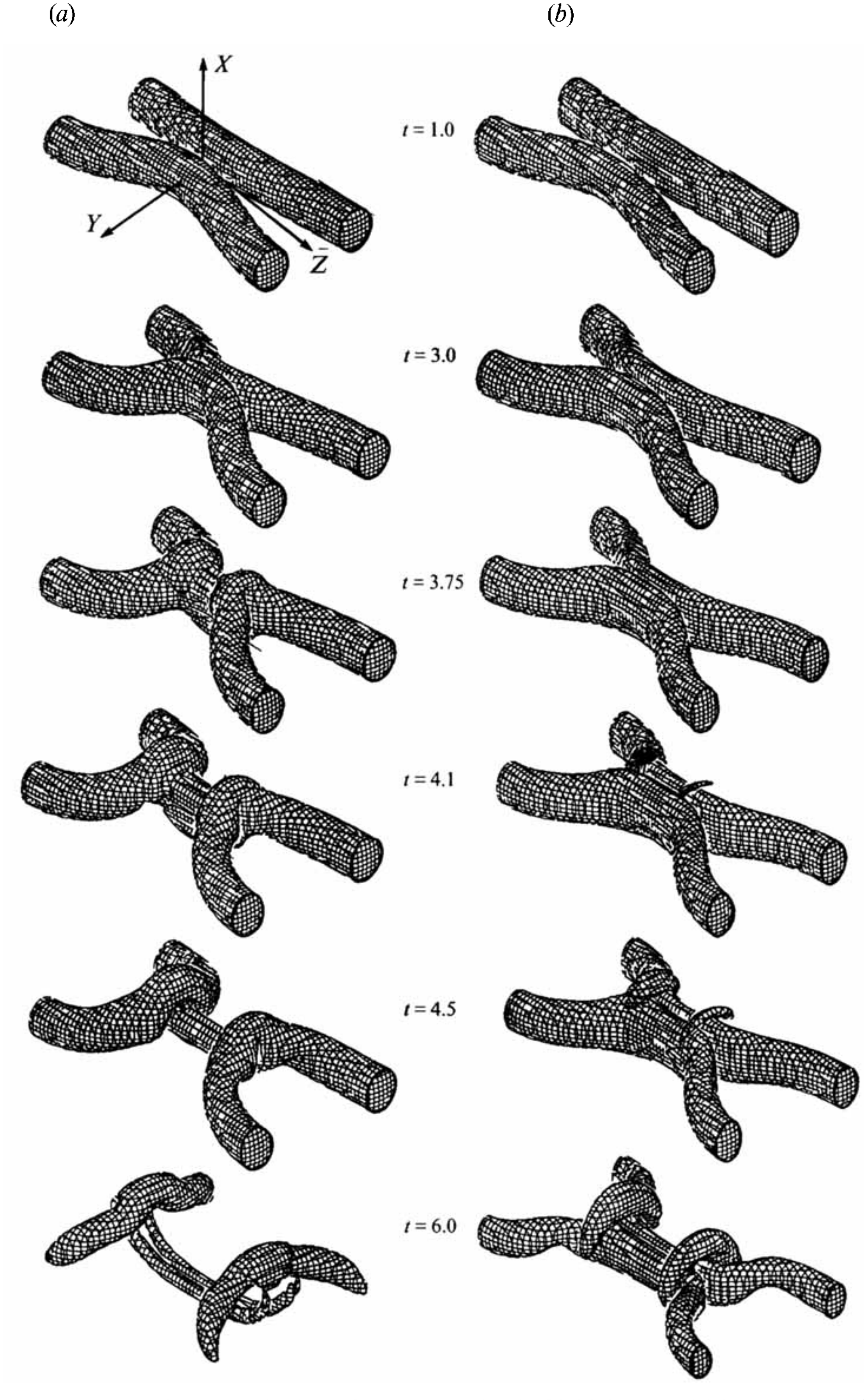

FIGURE 2. Isovorticity magnitude surfaces at 25% level of initial $|\omega|_{max}$. (a) low M (case A), (b) high M (case E). Circulation in π_s in case E at t=6.0 is the same as in case A at t=4.1.

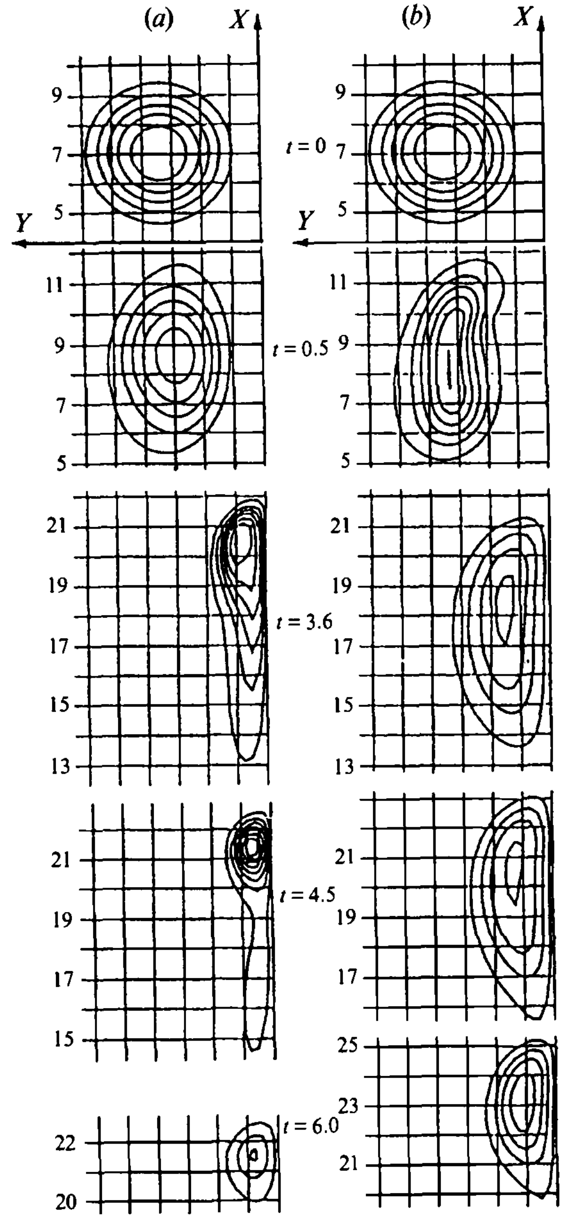

FIGURE 3. ω_z in π_s for cases A (*a*) and E (*b*). Every fourth grid line is shown. Minimum contour level is 1.0 and increment is 2.0.

remnants of the original vortex core in case E have higher $|\omega|$ and circulation (see §4.3) at $t = 6.0$, because of reduced reconnection (or circulation transfer) at higher M.

The vorticity contours in π_d show that the bridges have comparable Γ in both cases A and E by $t = 3.0$ (figure 4*a*). However, the bridge in case E is farther away from π_s. Since in both cases the self-induced motion of the bridges is directed away from π_s, we may infer that the bridging starts at an earlier time at high M (see figure 8*e*). This inference is supported by the results discussed in §4.3. At later times, we find that the bridges are stronger and have a more non-concentric vorticity distribution for low

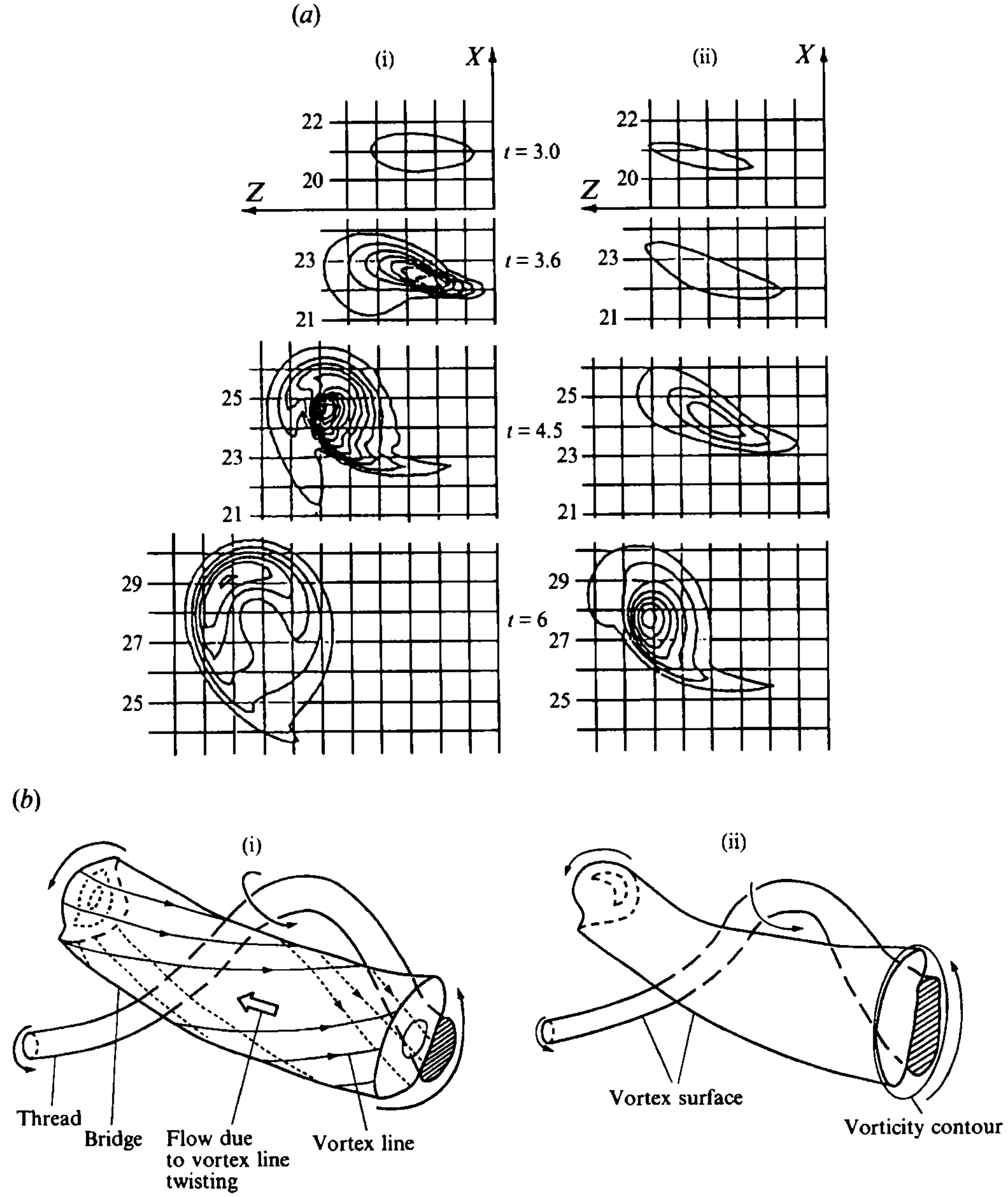

FIGURE 4. (*a*) ω_y in π_d for cases A (i) and E (ii). Every fourth grid line is shown. Minimum contour level and the increment are 1. (*b*) Two schematics of vortex tubes, in the quadrant simulated, see figure 1(*b*), to illustrate the cause and effect of non-concentric vorticity distribution in π_d. The first schematic shows twisting of vortex lines due to different vorticity magnitudes in π_d and the farthest computational plane parallel to π_s. The second schematic shows the distortion of vorticity contours in π_d to non-concentric distribution as a result of axial flow (due to vortex line twisting) and vortex stretching (by threads).

M. The sharp gradient in vorticity away from π_s after $t = 4.5$ for case A has been shown by Melander & Hussain (1990) to be due to stretching caused by the threads.

Local increases in $|\omega|$ due to vortex stretching by the threads play an important role in the bridges' internal dynamics. Consider a vortex tube representing a bridge as shown in figure 4(*b*). At locations where $|\omega|$ is larger the vortex lines rotate faster, thereby leading to overall twisting of vortex lines in the bridge. In turn, twisted vortex lines produce an axial flow along the vortex core, causing local vortex line compression and hence local reduction of $|\omega|$ (see §5.3). The radial vorticity gradient is larger in π_d where the vortex stretching due to the threads dominates and is smaller where the axial flow causes vortex line compression, thereby producing non-concentric vorticity contours. Based on these arguments, the nearly concentric vorticity contours at late times for case E are surprising because the threads are stronger than in case A and hence are expected to cause greater vortex stretching. Locally higher $|\omega|$ will cause greater twisting of vortex lines (i.e. stronger axial flow) and, consequently, more non-concentric vorticity contours. (Viscous diffusion would also tend to make vortices concentric. Since *Re* as well as the timescale of the simulations in both cases A and E are the same, viscous diffusion cannot be the primary cause of concentric contours at high M). Therefore, this observation suggests that compressibility effects are important even at late times and counter the local bridge stretching by the threads (see §5.3).

4.3. *Circulation transfer*

A quantitative measure of vortex reconnection is the transfer of Γ from π_s to π_d. In the following, we denote Γ in π_s by Γ_s and that in π_d by Γ_d. Figure 5(*a*) displays the evolution of Γ_s and Γ_d for all cases in table 1. The circulation transfer for the lowest M (case A) closely corresponds to the incompressible results of MH (1988). Initially in case A, Γ_s remains constant as the two interacting vortices approach π_d, followed by reconnection leading to a rapid decrease in Γ_s. This is followed by viscous decay of the threads at late times; during this time the circulation transfer rate is much slower since the threads' self-induced motion separates them.

As M increases, we note that there is a rapid transfer of Γ at around $t = 0.6$, with a transfer rate which increases with M. Then, the Γ transfer is reduced considerably and, for increasing M, is followed by delayed, increasingly slower transfer in the bridging phase. These observations are clear from the evolution of $\mathrm{d}\Gamma/\mathrm{d}t$ (in both π_s and π_d) shown in figure 5(*b*), where the first peak in transfer rate increases and the second peak decreases and is delayed for increasing M. In summary, we observe that with increasing compressibility effects, reconnection is initiated earlier (the early $\mathrm{d}\Gamma/\mathrm{d}t$ peak is due to a shocklet, discussed in §5.1) and is suppressed at later times in the bridging phase; i.e. the Γ transfer rate is slower, reaching a smaller maximum at a later time as M increases.

4.4. *Peak vorticity in π_s and π_d*

In figure 6(*a*), we show the evolution of peak vorticity in π_s for cases A–G. The fluctuations in the curves are due to the discrete grid, so that when the actual peak falls between grid points we observe a slight decrease. Unlike the incompressible simulations, we note that there are two peaks in vorticity evolution in π_s for sufficiently high M. However, as we discuss below, only the second peak is due to vortex stretching. The first peak is caused by a shocklet, entirely a compressibility effect (see §5.1.2). We also observe that as M increases, the second peak in vorticity is lower and is reached at a later time.

As Siggia (1985) observed an antiparallel configuration in vortex filament simulations just before severe vortex stretching ensued, antiparallel vortex tubes have been used to study the conjectured consequent finite-time singularity of the incompressible Navier–Stokes equations (Kerr & Hussain 1989; Pumir & Siggia 1990; Shelley *et al.* 1993). Since we also use an antiparallel configuration, the above results suggest

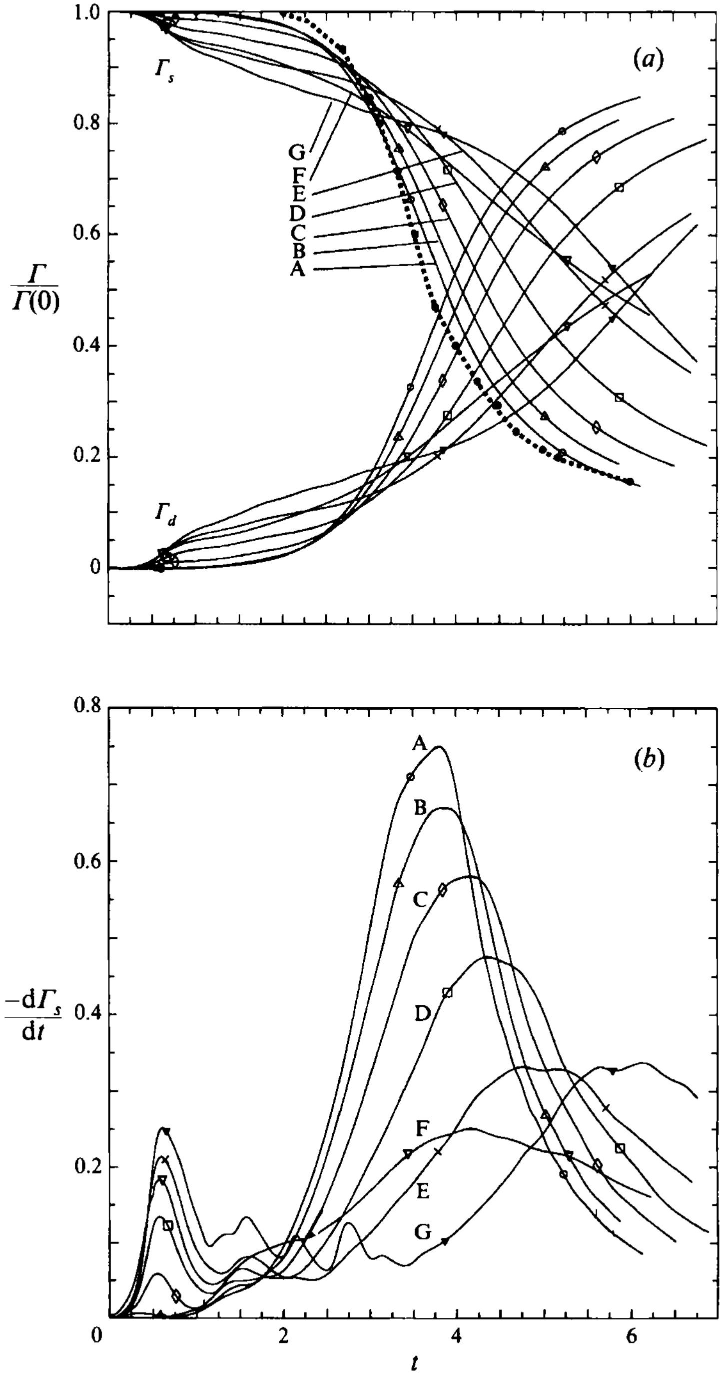

FIGURE 5. (*a*) Evolution of Γ_s and Γ_d normalized by initial Γ_s. (*b*) $-\mathrm{d}\Gamma_s/\mathrm{d}t$ ($=\mathrm{d}\Gamma_d/\mathrm{d}t$). Symbols are: ○, case A; △, case B, ◇, case C; □, case D; ×, case E; ▽, case F; ▼, case G. ●, incompressible data from MH (1988).

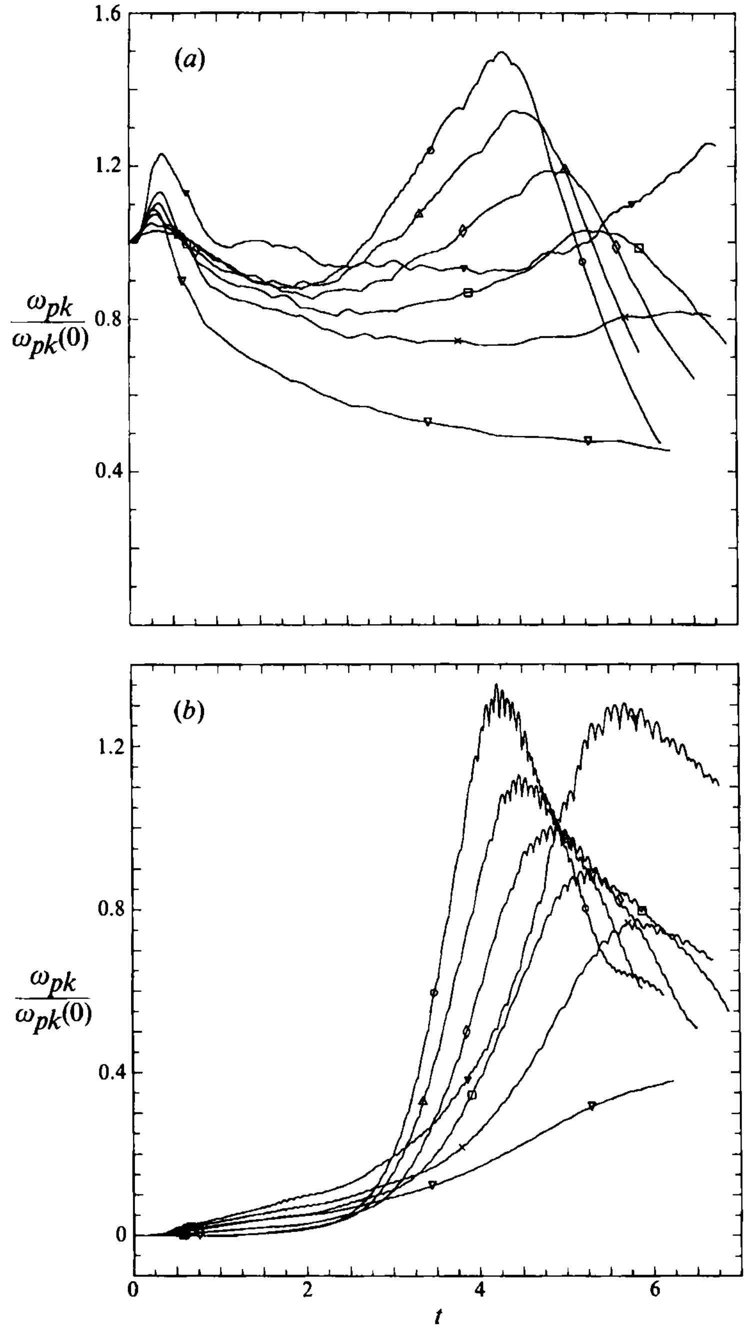

FIGURE 6. (*a*) Evolution of ω_{peak} in π_s normalized by its initial value. (*b*) Evolution of ω_{peak} in π_d normalized by the initial value of ω_{peak} in π_s. Symbols are the same as in figure 5.

suppression of this singularity, if it exists, by compressibility effects. The present results are, however, not conclusive as the peak vorticity increases with increasing *Re* for a given *M* (see figure 6*a*, cases E and G). In addition, we used lower *Re* in the compressible cases owing to the higher resolution required to resolve the shocklet (see §5.1).

The early evolution ($t < 3.0$) of peak vorticity in π_d shows that the vorticity first increases at a faster rate as M increases (figure 6*b*), consistent with the early bridging inferred from the Γ evolution. However, it reaches a lower maximum value and is delayed as M increases. This observation may appear inconsistent with the fact that the threads are much stronger in case E (see figure 2) and hence capable of causing higher vortex stretching in the bridges. However, the reduced peak vorticity in bridges at higher M is due to compressibility effects (see §5.3).

5. Compressibility effects

5.1. *Shocklet formation and its effects*

In order to understand the reason for early bridging and circulation transfer for high M, we consider motion of the vortex dipole in π_s in a reference frame moving with the dipole. Such a flow field has two stagnation points (S_F and S_R). In compressible simulations, we expect compression to occur as shown schematically in figure 7(*a*). The velocity divergence at $t = 0.1$ in case E, plotted in figure 7(*b*), is consistent with this expectation. If the velocity between the vortices is supersonic and decreases to subsonic (this is likely to occur near stagnation points seen in the moving reference frame), a shocklet can form where such a transition occurs. In figure 7(*c*) we show M in a laboratory reference frame, so the stagnation points are not seen, but the transition from supersonic to subsonic flow is clear.

A shocklet is characterized by a thin region of high negative dilatation (i.e. fluid compression). In figure 8(*a*), we show superimposed three-dimensional surface plots of $\nabla \cdot \boldsymbol{u} = -5.0$ and $|\omega| = 0.05$ at t=0.5 ($|\omega|_{max} = 11.17$ at this time). Dashed lines show P contours in π_s and π_d; in π_s, minimum P occurs near the vortex centre as expected, while in π_d, minimum P occurs before the shocklet (small X). In figure 8(*b*) we show cross-sections of this negative dilatation region with superimposed vorticity contours in π_s. It is clear that the shocklet (isodilatation surface) is curved and has non-uniform strength along both the Z- and Y-directions. This non-uniformity in shocklet strength is important for the baroclinically generated low-level vorticity seen behind (i.e. on top at larger X) the shocklet (see §5.1.2). Figures 8(*c*) and 8(*d*) show P (ρ is similar, not shown) and kinetic energy dissipation, respectively, in π_s at this time. Note the characteristic high gradient of P and large dissipation in the shocklet. In figure 8(*e*), we show kinetic energy dissipation and overlaid vorticity contours in π_d. Even at this early time, the presence of bridges is clear, indicating an earlier start of reconnection in case E.

To establish that the negative dilatation region observed in figure 8(*a,b*) is a shocklet, we compared the values of P, ρ and $\boldsymbol{u}$ on each side of this region along the X-axis (figure 9) with those expected from Rankine–Hugoniot relations for a normal shock (e.g. Thompson 1984, p.323). We use subscript '1' to denote the direction where fluid enters (before) the shocklet and '2' to denote where it exits (after), and define $w_1 \equiv -(\boldsymbol{u}_1 - \boldsymbol{b}) \cdot \boldsymbol{n}_1$, $w_2 \equiv (\boldsymbol{u}_2 - \boldsymbol{b}) \cdot \boldsymbol{n}_2$, where $\boldsymbol{b}$ is the shocklet velocity and $\boldsymbol{n}_1$ and $\boldsymbol{n}_2$ are outward normals, and $M_{1n} = w_1/c_1$ is the normal Mach number before the shock. Along the X-axis, only the X-component of velocity is non-zero; so we can readily use normal shock relations. Since there are three relations and seven unknowns (P, ρ and $\boldsymbol{u}$ before and after the shocklet and its speed), we obtain P_1, ρ_1, $\boldsymbol{u}_1$ and P_2 directly from the simulation data ($P_1 = 0.50288$, $\rho_1 = 0.46504$, $\boldsymbol{u}_1 = 1.9144$, $P_2 = 1.0118$). The shocklet boundaries were taken as the locations where the velocity showed a sharp change, and the same grid point was used to read the values of all

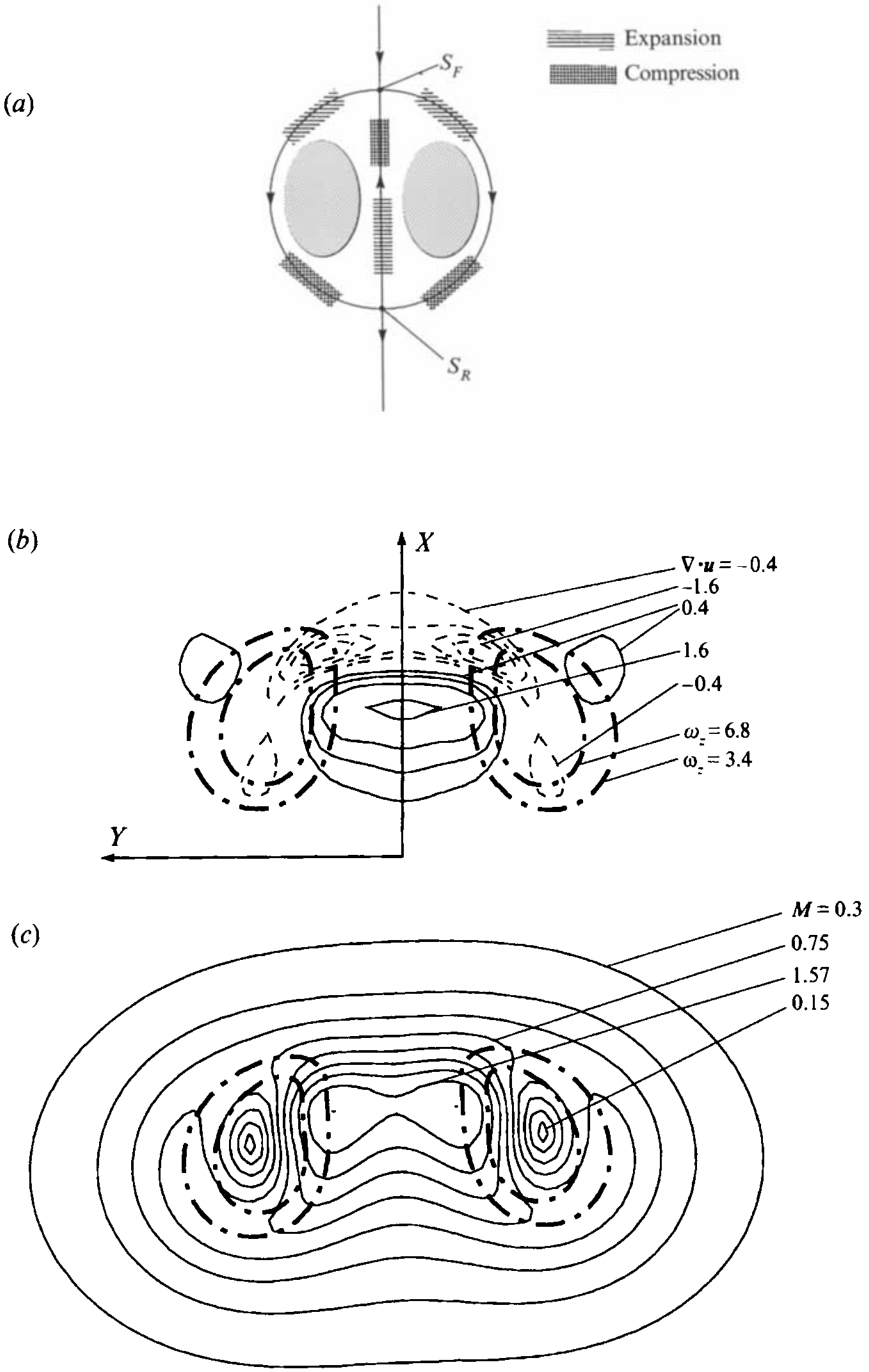

FIGURE 7. (*a*) Schematic of the vortex dipole in π_s in a moving reference frame to show the expected regions of compression and expansion. (*b*) $\nabla \cdot \boldsymbol{u}$ in π_s at $t = 0.1$ for case E. Chain-dashed lines are ω_z contours. (*c*) M at $t = 0.1$ in π_s for case E. The same ω_z contours as in (*b*) are overlaid for reference.

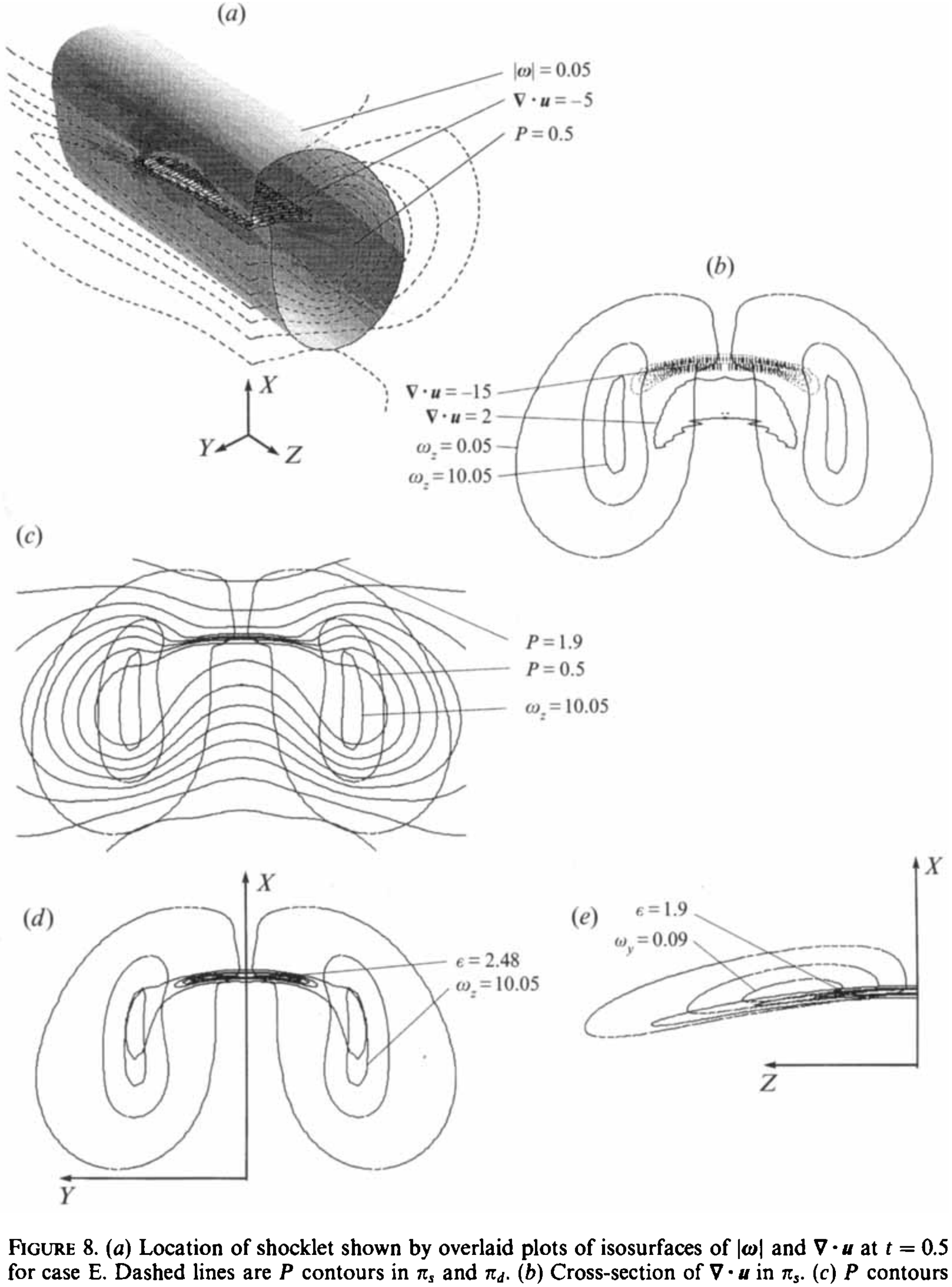

FIGURE 8. (*a*) Location of shocklet shown by overlaid plots of isosurfaces of $|\omega|$ and $\nabla \cdot \boldsymbol{u}$ at $t = 0.5$ for case E. Dashed lines are P contours in π_s and π_d. (*b*) Cross-section of $\nabla \cdot \boldsymbol{u}$ in π_s. (*c*) P contours in π_s. (*d*) Kinetic energy dissipation ($\epsilon = 2\nu D_{ij}D_{ij}$) in π_s. The ω_z contours are repeated in (*b–d*) for reference. (*e*) Kinetic energy dissipation in π_d. Overlaid contours of ω_y clearly show the location of bridges.

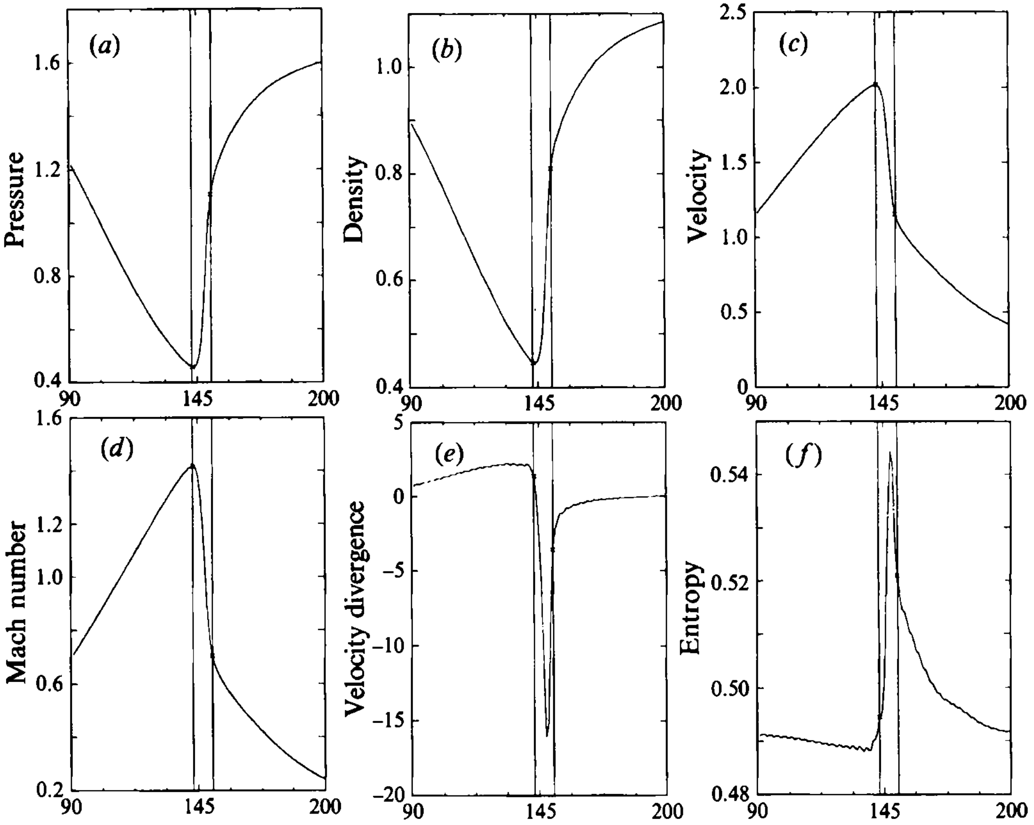

FIGURE 9. Property variations across the shocklet, along the X-axis, at $t = 0.5$ for case E. (*a*) P, (*b*) ρ, (*c*) u, (*d*) M, (*e*) $\nabla \cdot \boldsymbol{u}$, (*f*) Entropy (=log (V/V_o) + $(1/\gamma)$ log (P/P_o); where P_o and V_o are reference pressure and specific volume, respectively).

other quantities. Using the Rankine–Hugoniot relations, we estimated ρ_2 and $\boldsymbol{u}_2$ and the shocklet speed. Along the X-axis, the estimated $\rho_2 = 0.75874$ and $\boldsymbol{u}_2 = 1.2635$ are within 2% of the values observed ($\rho_2 = 0.75539$, $\boldsymbol{u}_2 = 1.2388$) in the simulation (figure 9); the shocklet speed b is 0.23299. Other typical characteristics of a shocklet, such as high negative dilatation and an increase in entropy across the shock, with an entropy peak inside the shocklet due to reversible viscous work (Lee *et al.* 1991), are also seen in figure 9. The plots of $\nabla \cdot \boldsymbol{u}$ and s show the Gibbs phenomenon near the shocklet, which is resolved with five grid points in the gradient region; the figures do not change (except for a more conspicuous Gibbs phenomenon) when the resolution in the X direction is halved. At lower M, the Gibbs phenomenon is absent from all curves. Even in the presence of the Gibbs phenomenon, the flow away from the shocklet is well resolved, and the total energy is conserved.

A shock is usually idealized as a discontinuity; however, it in fact has a finite thickness owing to viscous effects. For weak shocks, i.e. $M_{1n} - 1 \ll 1$, the shock thickness can be estimated as (Thompson 1984, p.364)

$$\delta \approx \frac{8}{3}\frac{\mu'}{\rho_1 c_1 (M_{1n} - 1)}, \tag{7}$$

where $\mu' = \mu + 3\mu_v/4$, μ is molecular viscosity, μ_v is bulk viscosity, and ρ_1 and c_1 are density and the speed of sound, respectively, before the shock. For the observed shocklet, $M_{1n}=1.366$, and we find that the distance between points 1 and 2 as defined in the previous paragraph is 4.3% higher than the value estimated using (7). Thus, a shocklet clearly has formed between the two vortices and can be resolved using global spectral methods.

5.1.1. *Shocklet location*

Before discussing the effects of this shocklet on reconnection, we point out that the shocklet observed in our simulation is at a different location than that suggested by Heister *et al.* (1990), based on an isentropic, inviscid analysis of a two-dimensional compressible dipole. These authors predicted that a shock would form in the compression regions near the rear stagnation point in figure 7(*a*), contrary to the shock observed in the compression region near the front stagnation point. This discrepancy is not likely to be due to three-dimensionality of reconnecting vortices, since the flow is approximately two-dimensional in and near π_s. Also, the simulations of a two-dimensional dipole in π_s discussed in §5.2.1 show a shocklet near the front stagnation point. Perhaps the discrepancy arises because Heister *et al.* used two point vortices with vacuum cores to construct the compressible vortex dipole and assumed isentropic flow. Moreover, the location of the shock was not ascertained from the P, ρ or the velocity divergence fields. Thus, further development of a compressible vortex dipole model at high M is needed, which should include a shock near the front stagnation point. It is interesting to note that when a supersonic jet is started, a vortex ring forms with a normal shock inside it (Baird 1987). The configuration in a meridional plane of the ring is similar to that in π_s for our case. The Broadbent & Moore (1987) model of this phenomenon perhaps should be the starting point for further analysis of a two-dimensional dipole.

5.1.2. *Shocklet-induced baroclinic vorticity generation*

To analyse the effect of the shocklet on early vortex reconnection dynamics ($t < 1$), we consider the enstrophy equation

$$\frac{\mathrm{D}(\frac{1}{2}\boldsymbol{\omega}\cdot\boldsymbol{\omega})}{\mathrm{D}t} = \underbrace{\boldsymbol{\omega}\cdot(\boldsymbol{\omega}\cdot\nabla)\boldsymbol{u}}_{\mathrm{I}} - \underbrace{\boldsymbol{\omega}\cdot\boldsymbol{\omega}(\nabla\cdot\boldsymbol{u})}_{\mathrm{II}} + \underbrace{\frac{1}{\gamma M_o^2}\boldsymbol{\omega}\cdot(\nabla P\times\nabla V)}_{\mathrm{III}} + \underbrace{\mu V\boldsymbol{\omega}\cdot\nabla^2\boldsymbol{\omega}}_{\mathrm{IV}}$$

$$-\underbrace{\mu\boldsymbol{\omega}\cdot(\nabla V\times(\nabla\times\boldsymbol{\omega}))}_{\mathrm{V}} + \underbrace{\tfrac{4}{3}\mu\boldsymbol{\omega}\cdot(\nabla V\times\nabla(\nabla\cdot\boldsymbol{u}))}_{\mathrm{VI}}. \qquad (8)$$

Among the four new terms (II, III, V and VI) on the right-hand side due to compressibility, only II and III are found to be significant in the present simulations. The magnitude of all terms in (8) at the location of peak vorticity in π_s at $t = 0.2$ is listed in table 2. Term II is obviously large in the shocklet, which is the location of high negative dilatation. From this table, it is clear that the early peak vorticity increase is governed by term II in (8), and that the vortex stretching is an order of magnitude smaller than the dilatation term. Thus, the first peak seen in figure 6(*a*) is due solely to compressibility effects. Physically, the increase in vorticity because of dilatation is due to concentration of the same circulation in a smaller material region due to fluid compression ($\nabla\cdot\boldsymbol{u} < 0$). This effect does not introduce new circulation, unlike baroclinic generation (see (9)).

Term in eqn. (8)	Case E ($t = 0.2$)	Case E ($t = 3.6$)	Case A ($t = 3.6$)
I	5.92219	9.3987	100.072
–II	95.46982	4.13056	–3.1714
III	–0.24047	0.214088	–0.76634
IV	–61.5574	–13.52274	–103.4628
–V	–0.05876	–0.0335	+0.09507
VI	–0.096772	–0.02895	0.002367
Sum	39.439	0.1582	–7.2311

TABLE 2. Enstrophy production terms at ω_{peak} in π_s

Interestingly, term III, which represents baroclinic vorticity generation, is also large near the shocklet. Initially, term III is identically zero as $P \propto \rho^\gamma$. At $t = 0.5$ (the time for figures 8 and 9), we show the three-dimensional isosurfaces of dilatation and $|B_T| = |(1/\gamma M_o^2)\nabla P \times \nabla V|$ (the baroclinic source term III) in figure 10(*a*). Since both quantities are large in the same spatial region, we show divergence on one side of π_d and B_T on the other. Cross-sections in π_s and π_d for these terms are shown in figures 10(*b*) and 10(*c*) respectively. In π_s, B_T is significant over the whole vortex core with alternate positive and negative regions. In the shocklet, B_T is mostly positive, with an internal patch of intense negative B_T. This negative region occurs due to the non-uniformity of the shocklet strength; the shocklet is strongest away from π_d, inside the vortex core.

In π_d, B_T is concentrated in the shocklet and is positive in the quadrant shown. This represents the generation of positive ω_y by baroclinic effects, in the same direction as vorticity in the reconnected configuration in this quadrant (only the ω_y component is non-zero in π_d). The dilatation $\nabla \cdot \boldsymbol{u}$ is negative in both quadrants, which also causes an increase in ω_y by term II in (8).

Flow behind a shocklet with non-uniform strength for an inviscid, steady flow is expected to be rotational due to baroclinic production of vorticity (Thompson 1984, p.74). A precise description of the baroclinic production in the present viscous and unsteady flow, however, is difficult. Nevertheless, figure 10(*a–c*) clearly shows alteration of the dipole vorticity and early baroclinic generation of bridge vorticity due to the shocklet.

5.1.3. *Effects of baroclinic vorticity*

To understand the effects of baroclinically generated vorticity, consider the evolution of Γ through a surface bounded by a material curve C:

$$\frac{\mathrm{d}\Gamma}{\mathrm{d}t} = \underbrace{\oint_C \frac{-1}{\gamma M_o^2} V\nabla P \cdot \mathrm{d}c}_{\text{Term 1}} + \underbrace{\oint_C \mu V \nabla^2 \boldsymbol{u} \cdot \mathrm{d}c}_{\text{Term 2}} + \underbrace{\oint_C \frac{\mu V}{3} \nabla(\nabla \cdot \boldsymbol{u}) \cdot \mathrm{d}c}_{\text{Term 3}}. \qquad (9)$$

Term 1 is due to baroclinic production, term 3 is a viscous effect due to dilatation, and term 2 is the usual incompressible viscous diffusion term. Here, π_s and π_d are material planes because the normal velocity in these planes is zero, and periodicity in the X-direction implies that the same fluid remains in these planes. In figure 11(*a*), since integrals along $a - b$ and $c - d$ in π_s cancel due to periodicity and that along $d - a$ is negligible since it is far removed, we can approximate the contour integral by

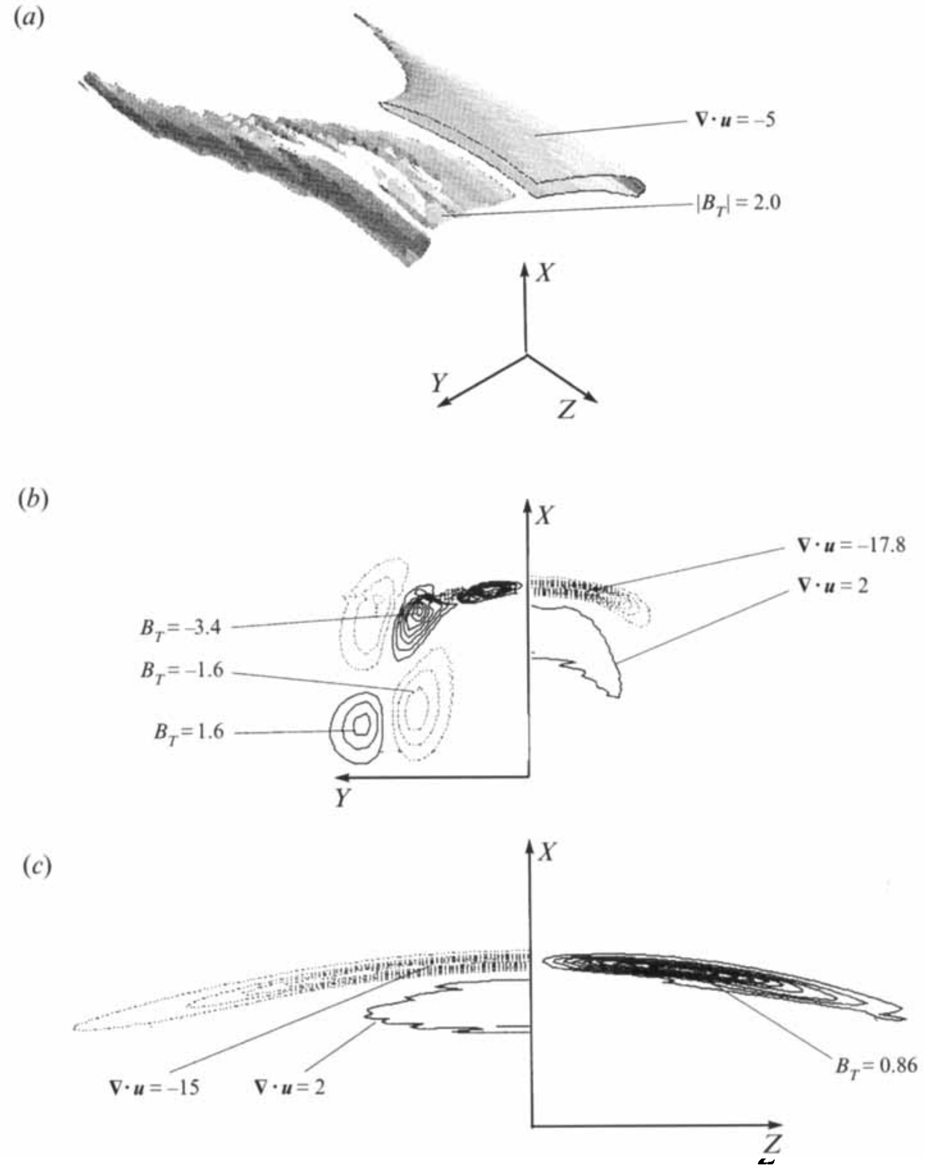

FIGURE 10. (*a*) Isosurfaces of $\nabla\cdot\boldsymbol{u}$ and $|B_T| = |\nabla P \times \nabla V|(1/\gamma M_o^2)$ at $t = 0.5$ for case E. The baroclnic production is large in the same region as dilatation which represents the shocklet. (*b*) Cross-section of (*a*) in π_s. Contour levels (min., max., increment) are: $\nabla\cdot\boldsymbol{u}$ (−17.8, 2, 3) on the right-hand side, B_T (−3.47, 3.4, 0.6) on the left-hand side. (*c*) Cross-section of (*a*) in π_d. Contour levels are: $\nabla\cdot\boldsymbol{u}$ (−15, −2, 3) on the left-hand side, B_T (0.866, 0.07, 0.07) on the right-hand side.

that along $b-c$, i.e.

$$\frac{\mathrm{d}\Gamma_s}{\mathrm{d}t} \approx \int_b^c \frac{-1}{\gamma M_o^2} V \frac{\partial P}{\partial x}\mathrm{d}x + \int_b^c \mu V \frac{\partial^2 u}{\partial x^2}\mathrm{d}x + \int_b^c \frac{\mu}{3} V \frac{\partial(\nabla\cdot\boldsymbol{u})}{\partial x}\mathrm{d}x \approx -\frac{\mathrm{d}\Gamma_d}{\mathrm{d}t}. \qquad (10)$$

The last approximation follows from the corresponding integration in π_d and is also justified by the data in figure 5(*b*). The magnitudes of the three terms in (9) are listed in table 3 for various M at an early time (when the shocklet exists for case E as shown

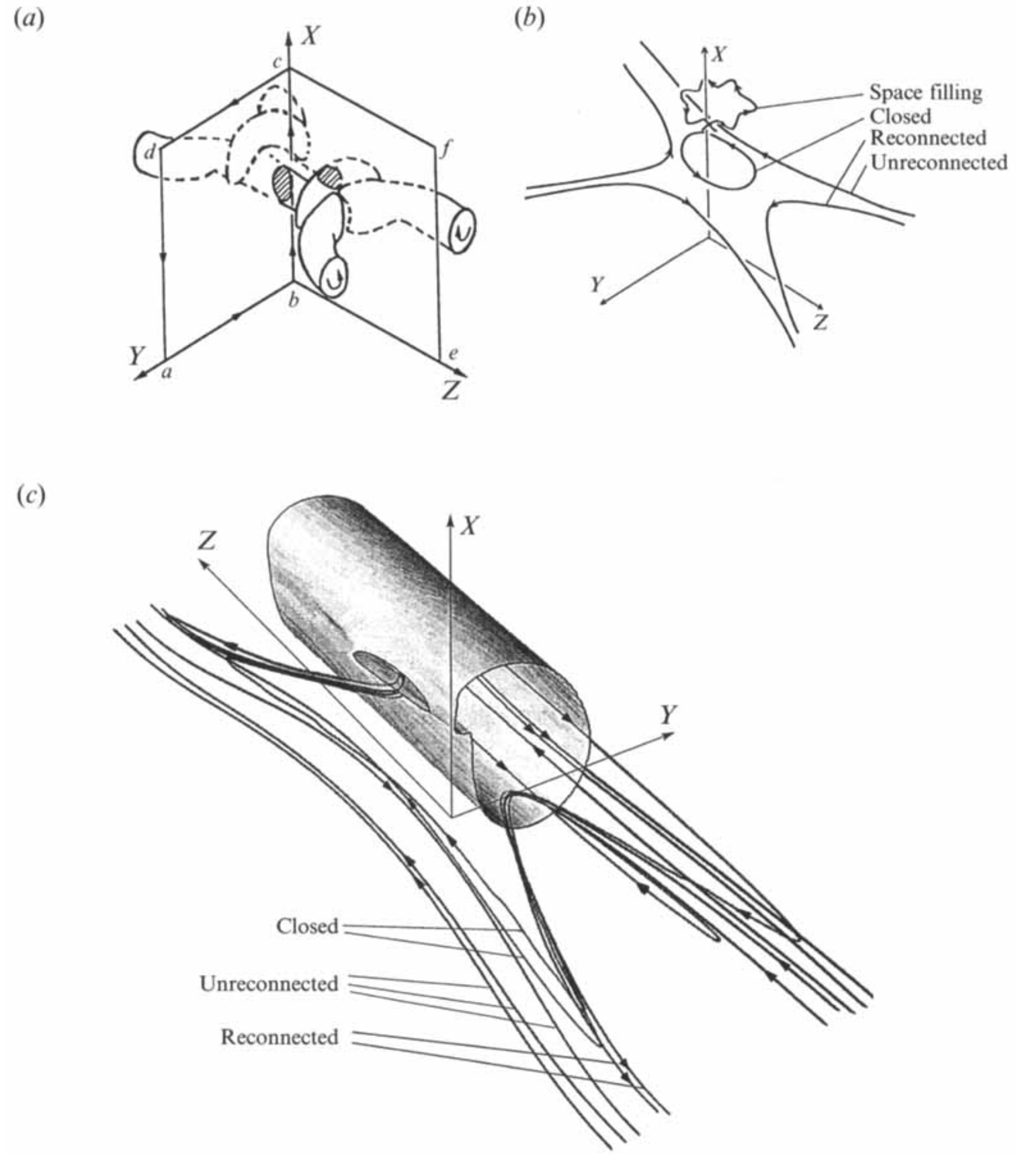

FIGURE 11. (*a*) Sketch of contour integrals to calculate the circulation transfer rate in π_s and π_d. (*b*) Sketch of possible topologies which satisfy (10). (*c*) Vector lines of $(\nabla P \times \nabla V)/\gamma M_o^2$ with an isosurface of $|\omega|$ overlaid at $t = 0.5$ for case E.

in the introduction to §5.1). At low M, $\mathrm{d}\Gamma_s/\mathrm{d}t$ is small, as expected. In case E, we note that $\mathrm{d}\Gamma_s/\mathrm{d}t$ has high contributions from both baroclinic and viscous effects. The increase in viscous effects with M is expected owing to the enhancement of vorticity gradients in π_s by the shocklet (see figure 3). Thus, the shocklet is responsible for early circulation transfer through baroclinic vorticity generation in π_d and baroclinic vorticity destruction in π_s, in addition to circulation transfer by enhanced viscous cross-diffusion.

Equation (10) implies that the changes in Γ_s and Γ_d are equal and opposite. Besides the cut-and-connect of an equal number of vortex lines, this is possible via

Re	1000	1000	1000	1000	1000	1500
M	0.5	0.95	1.14	1.28	1.45	1.45
Term in eqn (9)	Case A t=0.45	Case B t=0.55	Case C t=0.50	Case D t=0.55	Case E t=0.53	Case G t=0.53
1	-1.8×10^{-4}	-1.5×10^{-3}	-0.0245	-0.0628	-0.0893	-0.1295
2	-3.3×10^{-4}	-1.3×10^{-3}	-0.0256	-0.0558	-0.0838	-0.0780
3	-1.9×10^{-5}	-3.2×10^{-4}	-8.3×10^{-3}	-0.0181	-0.0274	-0.0259
Sum	-5.3×10^{-4}	-3.1×10^{-3}	-0.0584	-0.1367	-0.2005	-0.2334
$\mathrm{d}\Gamma/\mathrm{d}t$ in figure 5(*b*)	-5.9×10^{-4}	-3.2×10^{-3}	-0.0582	-0.1366	-0.2004	-0.2320
Term in eqn (9)	Case A $t=3.59$	Case B $t=3.53$	Case C $t=3.68$	Case D $t=4.57$	Case E $t=4.49$	Case G $t=5.51$
1	-0.0032	-0.0143	-0.0179	-0.0145	-0.0200	-0.0292
2	-0.6424	-0.5764	-0.4908	-0.4202	-0.2906	-0.2819
3	-2.3×10^{-5}	-2.3×10^{-4}	-4.1×10^{-4}	-4.5×10^{-4}	-5.8×10^{-4}	-7.3×10^{-4}
Sum	-0.6456	-0.5909	-0.5091	-0.4352	-0.3112	-0.3118
$\mathrm{d}\Gamma/\mathrm{d}t$ in figure 5(*b*)	-0.7301	-0.6342	-0.5373	-0.4660	-0.3204	-0.3276

TABLE 3. Circulation transfer terms in π_s

formation of closed vortex lines. Note that the vortex lines which cross π_s (or π_d) must extend to infinity, be closed, or densely fill a compact region (figure 11*b*). Only lines extending to infinity (i.e. reconnected or unreconnected lines) are possible in the incompressible case. Space-filling vortex lines cannot occur in our simulations owing to imposed symmetries. Closed vortex lines are impossible in incompressible antiparallel vortex reconnection because that would require two reconnections along a vortex line; incompressible vortex reconnection is possible only on the X-axis (i.e. at one point only). However, closed vortex lines representing a new topology are possible in a compressible antiparallel configuration; this is because baroclinic generation creates new vorticity and hence the topology change is, in principle, not restricted to cut-and-connect on the X-axis.

Since it is not possible to isolate baroclinically generated vorticity from the total vorticity field in a given flow field, we plot the vector lines of the baroclinic source term ($\nabla P \times \nabla V$) for case E to determine the topology of the baroclinically generated vorticity. However, the baroclinic term is a rate of change of vorticity which represents vorticity only after time integration. Thus, the vector lines in figure 11(*c*) represent baroclinic vorticity integrated over a small time. We do find closed vector lines, which suggests the possibility of closed vortex lines when baroclinic production is the dominant effect. By comparing high-M cases (E and G in table 3), we see that as *Re* increases, the baroclinic term indeed contributes more to circulation transfer than the viscous term; presumably, *Re* is not high enough for closed vortex lines to appear.

From (9), another important implication of baroclinic vorticity generation is that in compressible or stratified flows, reconnection can occur even in inviscid flows! But with the PIC used here, baroclinic generation is impossible without viscous terms as $\mathrm{D}(P V^{-\gamma})/\mathrm{D}t = 0$ for inviscid flows. Therefore, the reconnection in our simulations is necessarily a viscous event.

5.2. *Influence of shock-induced bridging*

At early times ($t < 2$), mutual induction of the vortex dipole in π_s reduces as M increases because of lower Γ_s and a stronger opposing flow induced by Γ_d due to early, shocklet-induced bridging. As a consequence, growth of the initial sinusoidal perturbation of the vortex tubes at later times is reduced as M increases. We now show this quantitatively by considering the motion of the vorticity centroids in π_s and π_d.

5.2.1. *Centroid motion*

To model the effects of bridges and time-varying strain rate based on the curvature of the interacting vortex tubes, we analyse the motion of vorticity centroids in π_s (x_s, y_s) and in π_d (x_d, y_d). Their evolution is shown in figure 12(*a,b*) for cases A and E. In π_s, we note that x_s for case E is smaller than that for case A until about $t = 4.0$, so that growth of the initial perturbation is lower for the high-M case. At very late times ($t > 4$) when Γ_s has reduced considerably, we find that x_s for case A actually lags that for case E owing to the much smaller Γ_s in case A than case E. The y_s motion shows that owing to lower curvature (since growth of the initial perturbation is slower), self-induced motion towards π_d is less in case E for all $t > 0.1$, as expected. Between $t = 1.5$ and 2.0 (for case A), Γ_s remains almost constant with increasing x_s. During this period, y_s decreases faster owing to higher self-induced motion of the interacting vortices towards each other.

In π_d, we find that the bridges move along the X-axis at nearly the same rate for both cases (figure 12*b*). Owing to noise-level vorticity in π_d at early times, the bridge centroid was calculated only after the peak vorticity in π_d was above 10% of the initial peak vorticity in π_s. By this time, the bridges have moved away from π_s in both cases, and thus we find that z_d is much larger than zero. At first sight, the decrease in z_d between $t = 1.5$ and $t = 4.0$ in case E and the almost constant distance from π_s between $t = 2.0$ and $t = 3.0$ for case A is surprising. To explain this, we note that there are two competing effects which determine z_d: (i) $\mathrm{d}\Gamma_d/\mathrm{d}t$ adds ω_y near X=0 thereby decreasing z_d, and (ii) self-induced motion of the bridges, which increases z_d. Thus, when effect (i) is dominant, the centroid moves closer to π_s. For high M, the self-induced motion of the bridges away from π_s is less since their curvature is small (see figure 2); i.e. effect (ii) is smaller than in case A. As a result, the final outward motion of the centroid in case E is delayed until there is sufficient Γ_d in the bridges to counter effect (i). But even after the outward motion of z_d starts, effect (ii) is small so that the motion is slower than in case A. The small peaks in $\mathrm{d}\Gamma/\mathrm{d}t$ are reflected as small fluctuations in z_d motion for case E between $t = 1$ and 2.5 (see figure 5*b*). For case A, between $t = 2.0$ and $t = 3.0$, effects (i) and (ii) balance, and we observe almost constant z_d. Thus, a model of compressible (as well as incompressible) vortex reconnection should account for both effects to accurately represent the bridge evolution, which is in turn crucial to successive reconnections.

Reduction of mutual induction in π_s As mentioned in the introduction to §5.2, there are two events which reduce X-direction vorticity centroid motion in π_s: (i) reduction of Γ_s, and (ii) flow induced by the bridges. In order to assess which of these events is dominant and when, we compare motion of the dipole in π_s with that of a two-dimensional dipole as follows.

First, consider a two-dimensional dipole with the same vorticity distribution as in π_s initially for the vortex reconnection simulations. The evolution of x_s for this case is shown in figure 13(*a*). Note that the high-M case moves slower than the low-M case. This effect is due to higher circulation annihilation in the high-M case presumably by enhanced vorticity gradients and baroclinic production due to the shocklet (see figure 13*b*), as in vortex reconnection. When we place the two vortices much farther apart, the evolution of x_s is the same for both high and low M (figure 13*c*). Although circulation decay is still higher in the high-M case, the decrease in

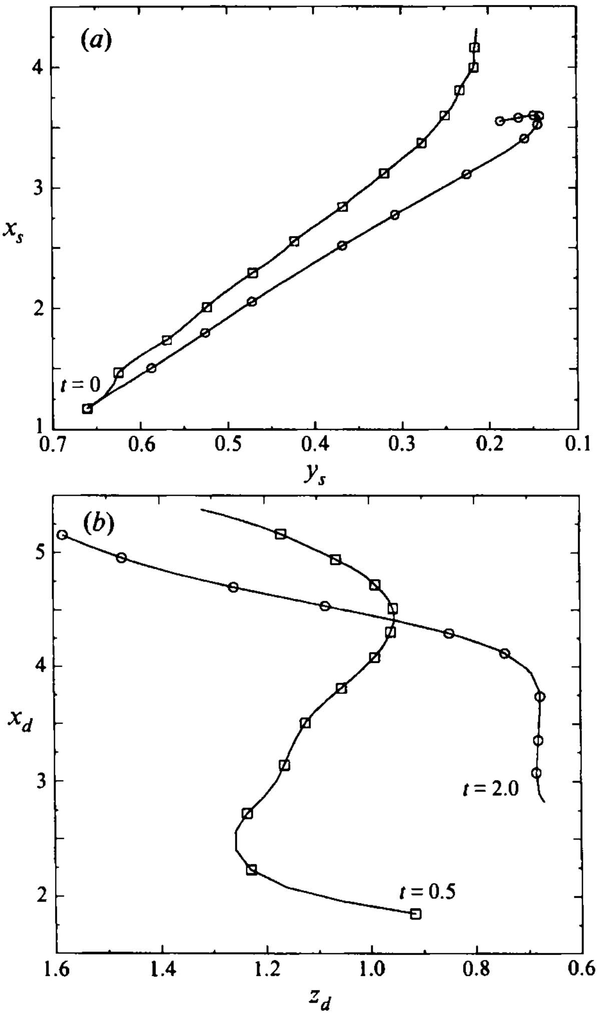

FIGURE 12. (*a*) Location of vorticity centroid in π_s. (*b*) Location of vorticity centroid in π_d. ○, denotes case A; and □, case E. The symbols are after every time increment $(\Delta t)=0.5$ until $t = 6.0$. For case A in (*b*) the first time is 2.0.

circulation is negligible (figure 13*d*). From this we conclude that compressibility effects can cause higher circulation annihilation, but for a given circulation, compressibility has a negligible effect on dipole propagation.

The propagation of a dipole constructed with two point vortices in an isentropic, subsonic, inviscid flow (where circulation remains constant) has been studied by Moore & Pullin (1987). Using perturbation analysis, they show that the reduction in steady propagation velocity is proportional to $M_\infty^2 = q_\infty^2/c_\infty^2$, where M_∞, q_∞ and c_∞ are Mach number, dipole velocity and speed of sound. They attribute this reduction to differences in the shape of the vacuum region (with increasing M_∞) which exists in the point vortex model of a compressible dipole. For our case, M_∞ is 0.12 and 0.3 in cases A and E, respectively (with q_∞ estimated from x_s evolution in figure 13*a*). Thus, the propagation reduction due to compressibility effects other than circulation annihilation (such as the shape of the vacuum region in the Moore & Pullin model) is very small in our case even though the flow in the dipole is supersonic.

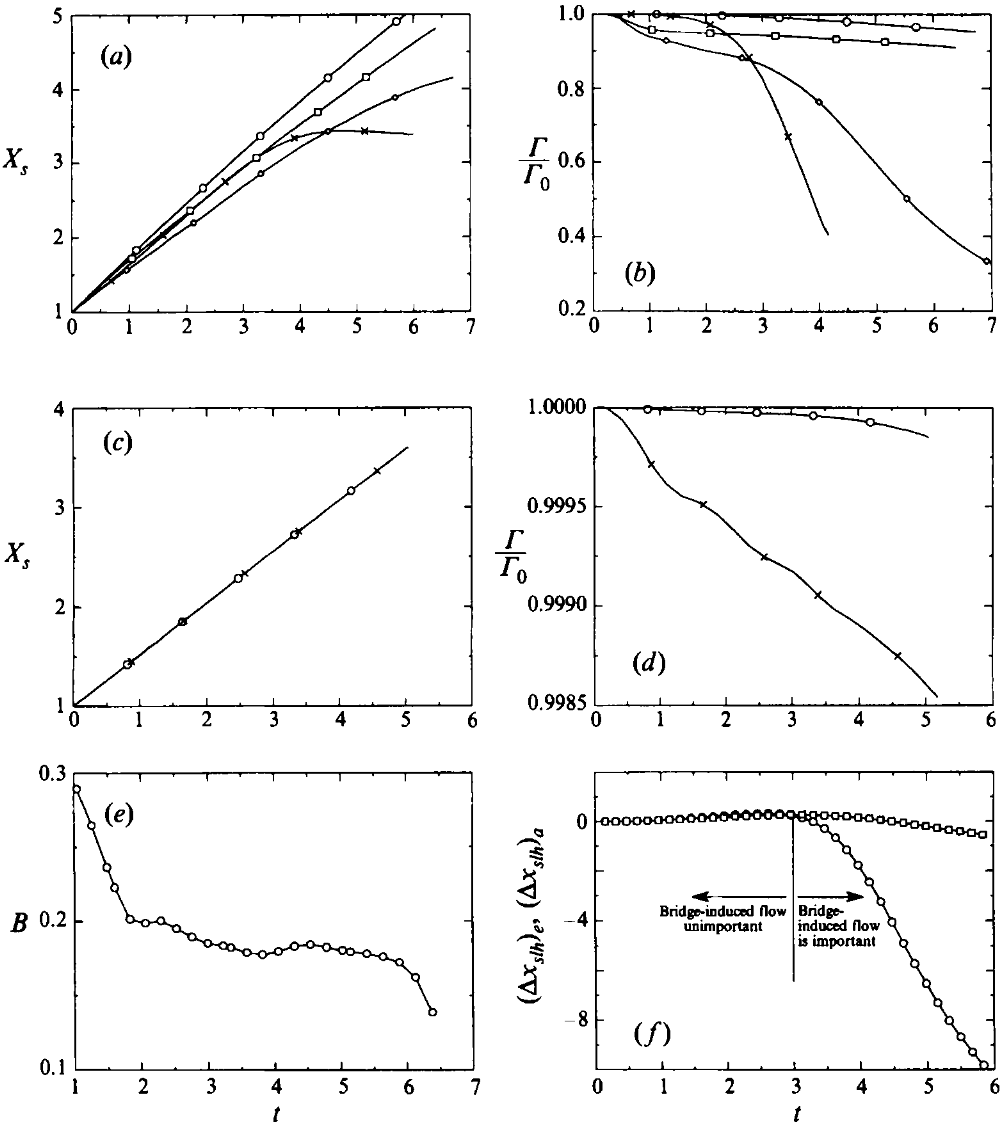

FIGURE 13. (*a*) Motion of centroid in π_s for case A (×), case E (◇), and two-dimensional dipoles initially arranged the same as π_s dipole in reconnection simulations: low M (○), high M (□). (*b*) Evolution of circulation for the cases in (*a*). (*c*) Motion of centroid of two-dimensional dipoles well separated initially: low M (○), high M (×). (*d*) Evolution of circulation for the cases in (*c*). (*e*) Evolution of B defined in (12). (*f*) $(\Delta x_{slh})_e$ (○) estimated and $(\Delta x_{slh})_a$ (□) observed differences in centroid locations for high- and low-M cases based on the two-dimensional model taking into account only the reduction in motion due to reduced circulation.

Based on the above results, we neglect compressibility effects (other than those causing circulation reduction) which reduce the dipole propagation. Therefore, to estimate the effects of bridges, we consider the dipole motion in π_s for cases A and E; the two cases have significantly different bridge evolutions, and their comparison helps to isolate the effects of bridges. Note that we do not compare compressibility effects here, i.e. this analysis could also have used, for instance, two incompressible cases at significantly different Re, where the bridges evolve on quite different timescales.

We consider only the change in π_s dipole propagation due to reduction in Γ_s (which includes both incompressible and compressible circulation-changing mechanisms) and the bridge-induced flow. The propagation velocity is expected to be proportional to Γ_s and inversely proportional to the distance between the dipole vorticity centroids. Therefore, we can write

$$x_s(t) \equiv \begin{array}{c}\text{Mutual induction}\\ \text{without annihilation}\end{array} + \begin{array}{c}\text{Reduction due to}\\ \text{loss of } \Gamma_s\end{array} + \begin{array}{c}\text{Reduction due to flow}\\ \text{induced by bridges}\end{array},$$

$$x_s(t) = A\Gamma_{s0}t + B\int_0^t \frac{\Gamma_{st}-\Gamma_{s0}}{y_s}\mathrm{d}t + C\int_0^t \frac{\Gamma_{st}-\Gamma_{s0}}{z_d}\mathrm{d}t, \tag{11}$$

where Γ_{s0}, Γ_{st} are circulations in π_s at t=0 and t respectively, y_s and z_d are the dipole radii in π_s and π_d, and A, B and C are constants.

Clearly, C is zero in the two-dimensional dipole case. We can estimate B from the two-dimensional dipole motion with the same initial vorticity distribution as in π_s for the vortex reconnection simulations (shown in figure 13a) from

$$x_{sl}(t) - x_{sh}(t) = B\left[\int_0^t \left(\frac{\Gamma_{st}-\Gamma_{s0}}{y_s}\bigg|_l - \frac{\Gamma_{st}-\Gamma_{s0}}{y_s}\bigg|_h\right)\mathrm{d}t\right], \tag{12}$$

where A cancels and subscripts l and h denote low- and high-M cases. The estimate of B is shown in figure 13(e). B is not precisely constant because the vortex core deforms during evolution, while the above model is valid only for an inviscid point-vortex. However, $B = 0.186$ is representative of most of the evolution. For an inviscid, incompressible point vortex dipole $B = 1/4\pi = 0.0795$.

It is difficult to estimate C in the same manner because z_d is not precisely defined when Γ_d is small, owing to noise-level vorticity. Since it is also difficult to measure A accurately, we use the above estimate of B to estimate the difference $(\Delta x_{slh})_e (= x_{sl}(t) - x_{sh}(t))$ in x_s between high- and low-M reconnection cases (this uses (12) with data for Γ and y_s from the reconnection simulations, i.e. neglecting the third term in (11)) and compare with the actual values $((\Delta_{slh})_a x)$. Let

$$DX = (\Delta x_{slh})_a(t) - (\Delta x_{slh})_e(t) = C\left[\int_0^t \left(\frac{\Gamma_{st}-\Gamma_{s0}}{z_d}\bigg|_l - \frac{\Gamma_{st}-\Gamma_{s0}}{z_d}\bigg|_h\right)\mathrm{d}t\right].$$

Both $(\Delta x_{slh})_e$ given by (12) and $(\Delta x_{slh})_a$ are shown in figure 13(f). When the two values differ in figure 13(f), the difference in the bridge-induced flow between cases A and E is important. DX is large after $t = 3.0$. Until $t = 2.0$, Γ_{st} in case A is larger by 10% (see figure 13a; virtually no bridging in case A), but DX is nearly zero, implying that when bridges are weak, their effect can be neglected. After $t = 3$ bridging in case A is rapid and Γ_{st} is smaller than in case E (figure 13b) and DX increases. Since bridge circulation does not change significantly between $2 < t < 3$ in case E, we can infer that the cause for increasing DX is the stronger bridges in case A. For $t > 3$, Γ_d in both cases A and E increases, but the increase in case E is much slower and this is reflected by increasing $|DX|$ in figure 13(f). Note, however, that this qualitative trend would be modified owing to the effect of the first term in (11) in increasing the propagation of the low-M dipole due to smaller y_s (see figure 12a), which is not included in the estimate for figure 13(f). This term need not be included in the estimate of B via (12) since y_s remains almost constant for the two-dimensional dipole.

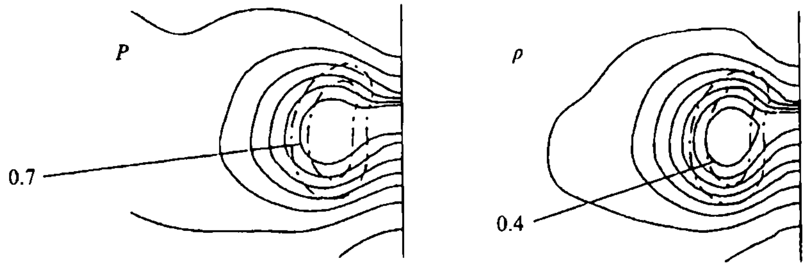

FIGURE 14. P- and ρ-contours in π_s at $t = 1.5$ for case E. The lack of high gradient regions shows the absence of a shocklet. Chain-dashed lines are ω_z contours for reference.

The motion of y_s is affected by that of x_s as follows. As x_s increases, the curvature of the interacting vortices increases, acting to decrease y_s faster owing to higher self-induced motion of the vortex tubes towards each other. This leads to higher annihilation of Γ_s, thereby reducing the rate of increase of x_s and hence counteracting the rate of y_s reduction.

At the time when DX begins to increase in figure 13(*f*), about 20% of Γ_s has been transferred to π_d. This analysis implies that the reconnection model of Saffman (1990), which neglects bridging, may hold only for early evolution when 80% of the circulation in π_s remains unannihilated. After this time, the effects of bridges on the reduction of dipole propagation in π_s should appear in Saffman's model as a change in the strain rate responsible for dipole radius reduction and also as additional induced flow which causes vortex stretching in π_s. Thus, by analysing the motion of x_s, we are able to clearly show the need for including the effects of bridging in a vortex reconnection model and to demonstrate the bounds of validity for Saffman's model.

5.2.2. *Shocklet diffusion*

By $t = 1.5$ the shocklet diffuses as shown by the lack of sharp gradients in the contours of P and ρ shown in figure 14 (compare with figure 8*c*). However, the flow is still locally supersonic in π_s. The primary cause of the disappearance of the shocklet is viscous diffusion, which acts to smooth the large gradients in velocity, P and ρ. Therefore, at higher Re the shocklet would persist for a longer time. We cannot perform simulations at much higher Re since the shocklet thickness would then be inadequately resolved (shock thickness decreases with viscosity, (7)). However, a preliminary check of this argument was made by considering $Re = 1500$ for doubled resolution in the X-direction. As expected, the shocklet was present for a slightly longer time as evidenced by the larger drop in Γ_s at early times (see figure 5*a*,*b*; case G). This of course raises the interesting possibility that Γ_s transfer due to a shocklet may be large enough at a significantly high Re so that complete compressible reconnection may occur on a much shorter timescale at high M (if based on a fixed extent of Γ_s transfer) than incompressible vortex reconnection. It is unclear how the bridge-induced flow will affect dynamics if the shocklet-induced Γ_s transfer were to exceed 20% of initial Γ_s.

5.2.3. *Reduced circulation transfer*

After the shocklet diffuses, the circulation transfer is primarily due to viscous cross-diffusion (as for incompressible vortex reconnection). This is clear from the magnitude of the circulation transfer terms at late times as shown in table 3. Viscous cross-diffusion is directly proportional to the vorticity gradient, which in turn is determined by the motion of the vortex tubes towards π_d. At high M, the self-induced motion of the vortex tubes toward π_d is decreased (as explained in §5.2.1) so as to reduce vorticity gradients in π_s. Thus, we observe that the circulation transfer rate has a lower peak (occurring at a later time) as M increases.

5.2.4. *Reduced vortex stretching*

As seen in figure 6(*a*), the peak vorticity in π_s is smaller at higher M. This is of relevance not only to possible singularity of the compressible Navier–Stokes equations, but also to modelling of compressible vortex reconnection. To determine the primary reason for this reduction in peak vorticity, we show the distributions of enstrophy production terms in π_s in figure 15 for cases A and E. Of the six terms on the right-hand side in (8), only the first four are significant. We observe that vortex stretching is more uniform over the cross-section in case E than case A. This is perhaps the reason for the lack of head–tail structure formation in case E. Values of all the terms at the location of ω_{peak} in π_s are given in table 2 at $t = 3.6$ for these cases. It is clear from this table that the reduction in peak vorticity is due to the considerably smaller (nearly a factor of 10) vortex stretching in the high-M case.

Vortex stretching in π_s is influenced by two effects: flow induced by the bridges and axial flow inside the vortex tube. Saffman's (1990) model considers only the latter effect partially: the flow due to the pressure gradient generated by cancellation of vorticity in the contact zone is considered; but axial flow due to vortex line twisting (Melander & Hussain 1994*b*) is neglected. For sufficiently high Re, the pressure drop across the cross-section of a rectilinear vortex is directly proportional to the square of axial circulation in that cross-section. Initially, the circulation is the same at all cross-sections, and thus there is no pressure gradient in the axial direction. At later instants, owing to transfer of Γ_s to Γ_d, the pressure drop across the cross-section is lower in π_s (and π_d) than for those parts of the vortex tube away from the interaction region. As a result, an axial pressure gradient is set up (figure 16*a*), which is proportional to the transferred circulation. At high M, the circulation transfer is reduced at late times owing to slower perturbation growth; thus the axial pressure gradient, and consequently, vortex stretching are smaller. We quantitatively show this by plotting the pressure gradient along the vortex line passing through the location of peak vorticity in π_s for cases A and E in figure 16(*b,c*). Near $Z = 0$, the maximum $|V\mathrm{d}P/\mathrm{d}s| \equiv |V\nabla P \cdot \omega/|\omega||$ is higher in the high-M case at early times $t = 0.1$ and 0.5, but is lower at late times $t > 4$. Since $-V\mathrm{d}P/\mathrm{d}s$ appears as the pressure gradient term in the momentum equation for velocity along a vortex line, a negative value of $V\mathrm{d}P/\mathrm{d}s$ implies induced flow away from π_s. The velocity gradient $\partial u_s/\partial s$ of this flow causes vortex stretching, where u_s is the velocity along the vortex line.

Vortex stretching in π_s is also induced by bridges (see figure 17*a*). Since bridges are much weaker for case E at late times, the vortex stretching due to this effect is also lower and this leads to lower peak vorticity as M increases for a given Re.

5.3. *Compressibility effects in bridges*

To determine the compressibility effects in bridges inferred in §4.2, we consider the dominant terms in the enstrophy equation (8). In figure 17(*b*) we show the contours of the four dominant terms in π_d. In case A, as observed by Melander & Hussain (1990), the vortex stretching term is negative over a part of the cross-section and has a large positive peak where the threads are closest to the bridges. The negative region is due to flow induced by the helical vortex lines. Compared to vortex stretching,

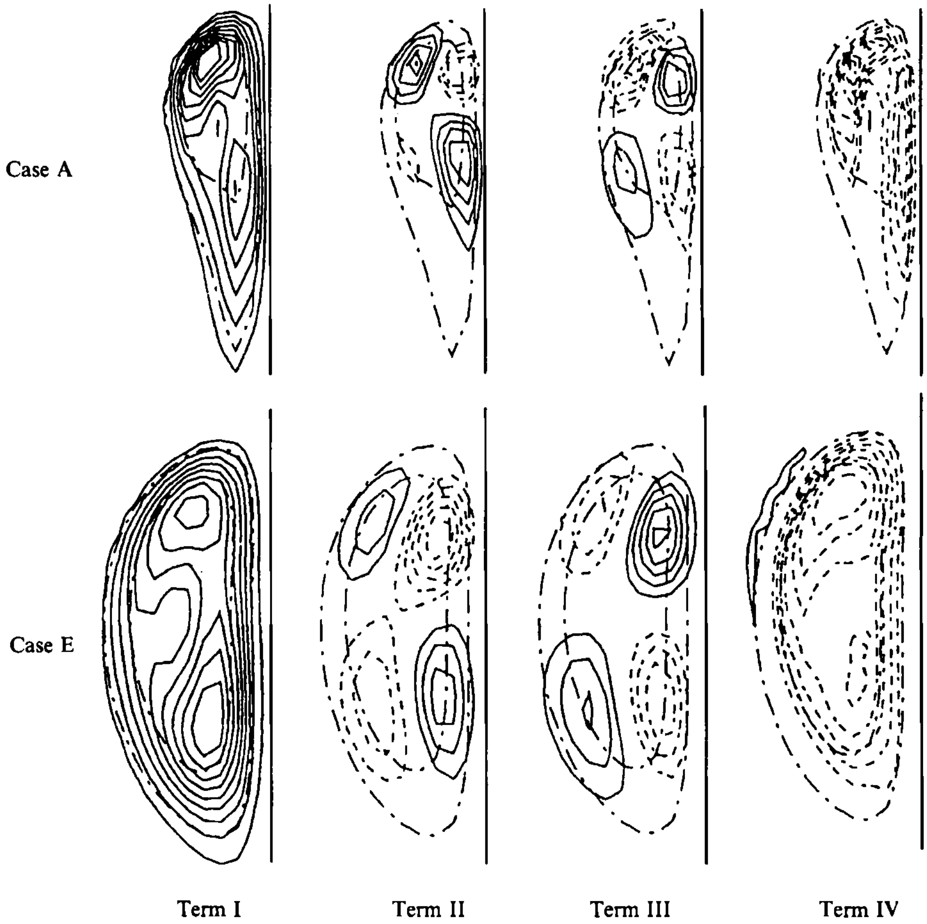

FIGURE 15. Enstrophy production terms at $t = 4.5$ in π_s. Contour levels (min., max.) with constant increment are: Case A: Term I (12.74, 127.45), Term II (−9.74, 10.66), Term III (−3.53, 2.27), Term IV (−134, 19.54). Chain-dashed lines are ω_z contours, negative contours levels are dashed lines and positive contour levels are solid lines. Case E: Term I (1.56, 15.6), Term II (−16.34, 8.95), Term III (−3.47, 3.57), Term IV (−14.82, 2.2).

the dilatation and baroclinic production terms are negligible in case A. In case E, the vortex stretching is higher than in case A, as expected from the stronger threads. In addition, the dilatation production is significant with a similar distribution, but reduces the peak vorticity. Thus, the local increase in $|\omega|$ in π_d in case E is less than in case A (see figure 6*b*), and the twisting of vortex lines in bridges is less, as is clear by comparing vortex lines in bridges in figure 17(*d*,*e*). In this figure, we have also overlaid parts of different levels of isovorticity surfaces to emphasize their differences with vortex surfaces. The vortex lines are generated by starting a rake at a contour of $|\omega|$ in π_s and the same contour in π_d; thus, near π_s and π_d vortex surfaces and isovorticity surfaces are very similar, but farther away, vortex lines cross isovorticity surfaces. Even though isovorticity surfaces mimic the topology of vortex surfaces, they fail to reveal the detailed features: for example, formation of hairpin-like structures in region C (figure 17*d*), or threads not being connected to the vortex centre away from the reconnection zone. The hairpin-like structure in region C in case A is formed owing to motion of thread vortex lines due to the flow induced by much

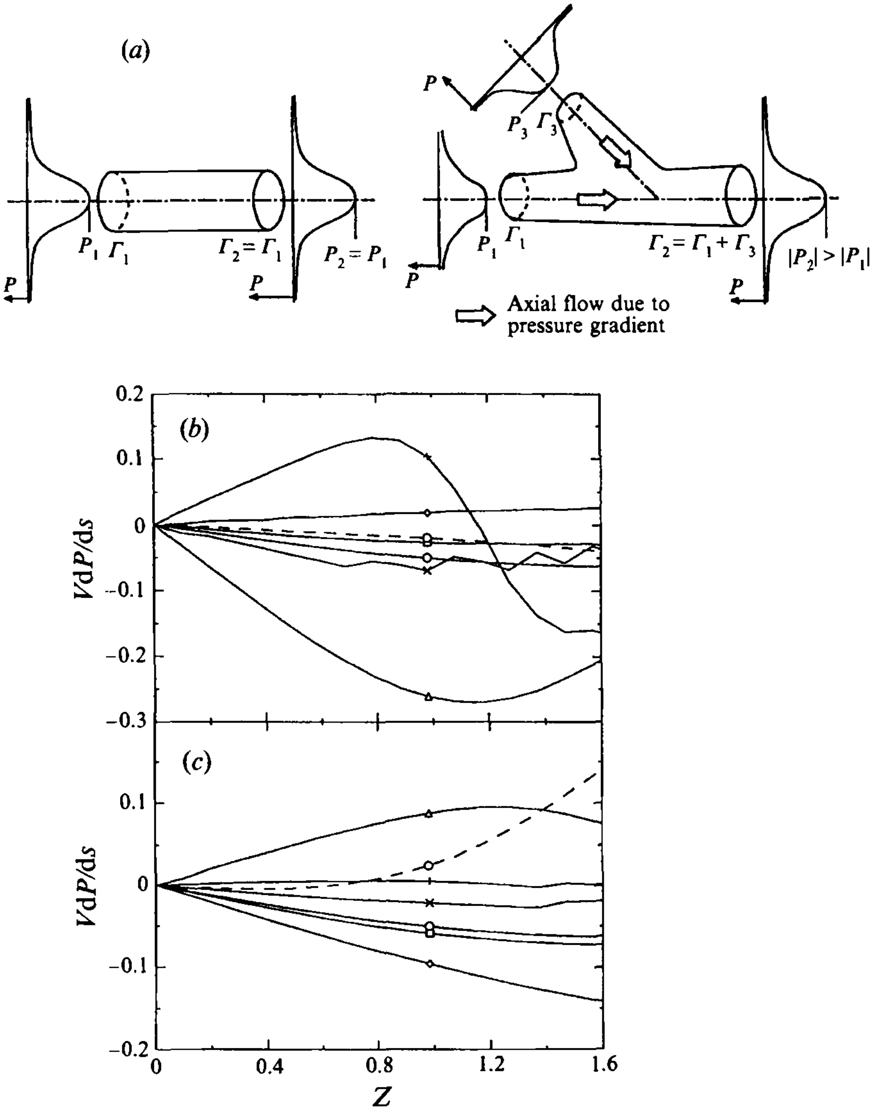

FIGURE 16. (*a*) Sketch to illustrate the reason for axial flow due to change in circulation in π_s. For a rectilinear vortex, the pressure drop is directly proportional to the square of the axial circulation. (*b*, *c*) VdP/ds along the vortex line starting at the location of ω_{peak} in π_s. (*b*) Case A and (*c*) case E. The symbols denote different times: ○, $t = 0.0$; □, $t = 0.1$; ◇, $t = 0.5$; ×, $t = 3.0$; +, $t = 3.6$; Δ, $t = 4.5$; –○–, $t = 6.0$.

stronger bridges. Unlike case A at late times, the bridges and threads in case E are of comparable strength, and thus, a hairpin-like structure does not form (figure 17*e*); the lack of hairpin formation is similar to case A at an earlier time (figure 17*c*). The twist of vortex lines in bridges (region A in figure 17*c*–*e*) leads to axial flow, as shown by a sketch in figure 4(*b*).

Even though at late times compressible vortex reconnection occurs primarily through (incompressible) viscous cross-diffusion, compressibility effects cannot be neglected as they suppress core dynamics (axial flow due to vortex line twisting) in the bridges.

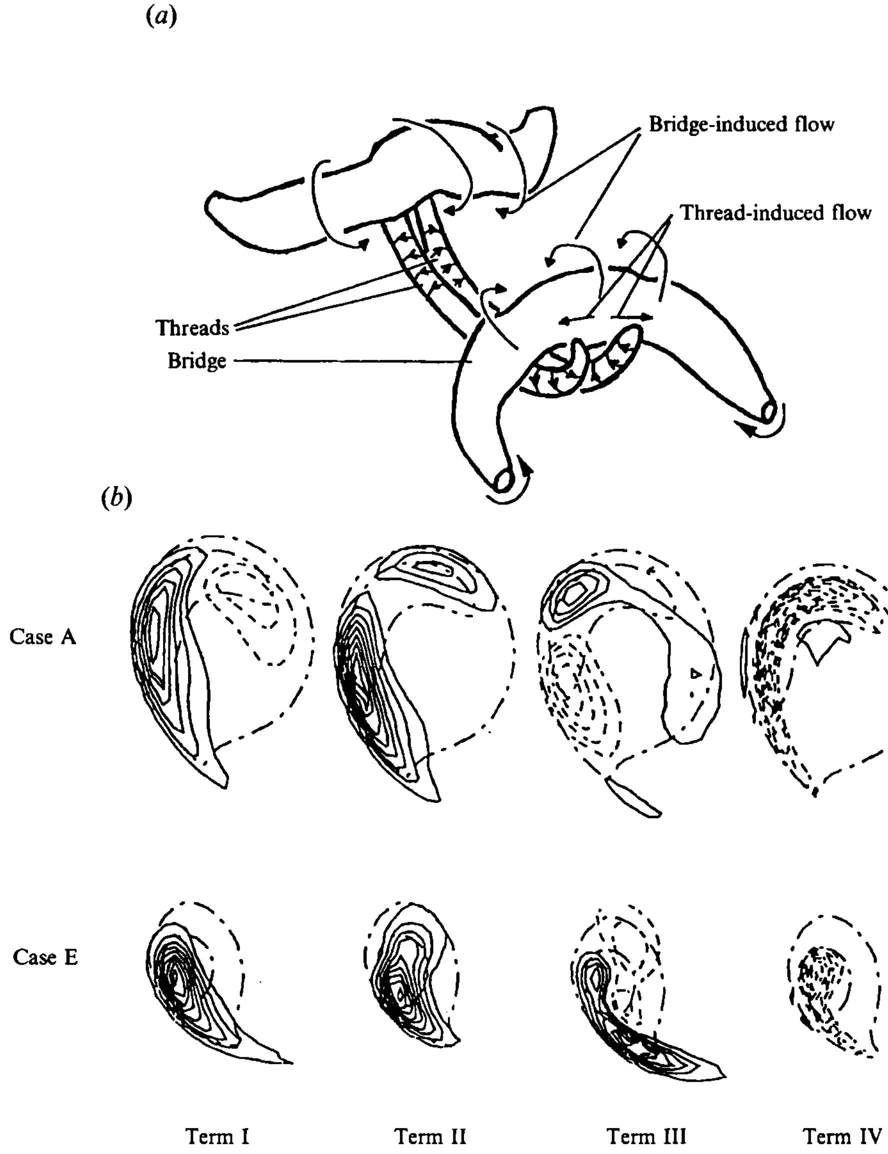

FIGURE 17 (*a*, *b*). For caption see next page.

5.4. *Effect of temperature-dependent* μ *and* κ

In most of our simulations, we assumed that μ and κ are constants, in order to economize computation (by about a factor of 4). However, we did run the highest-M case with $\mu/\mu_o = (T/T_o)^{0.76}$ and constant Pr in order to determine the effect of temperature dependent properties. The evolutions of Γ and peak vorticity in π_s and π_d are shown in figures 5(*a,b*) and 6(*a,b*) (compare cases E and F). The trends are similar in both the constant-property and the temperature-dependent-property runs. A slightly lower peak vorticity and a slightly higher circulation transfer are expected owing to a local increase in μ in the contact zone when the shocklet exists. Thus, the results with temperature-dependent properties are similar to that for a constant-property case at a slightly lower Re. Note that this observation is not expected to

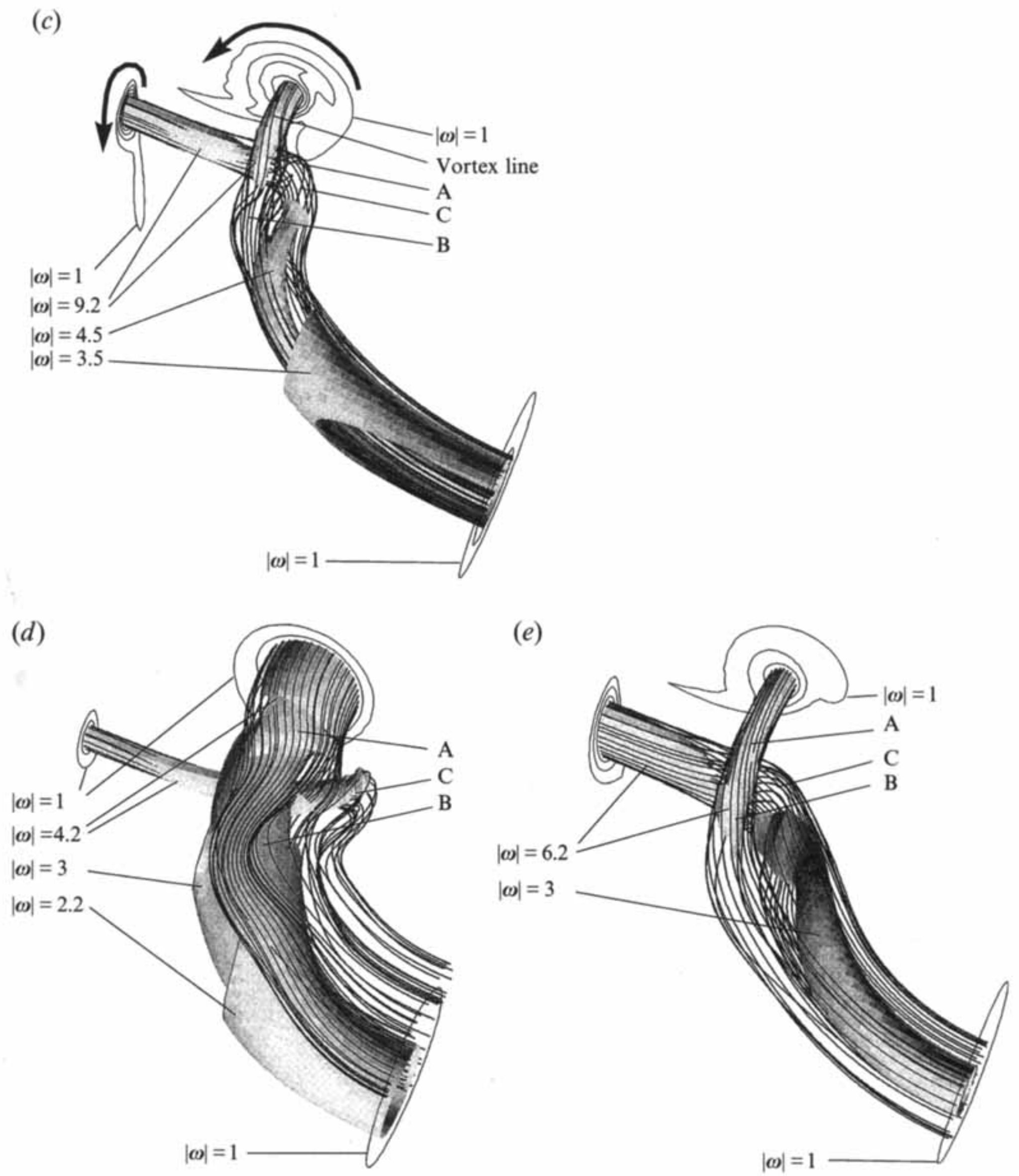

FIGURE 17. (*a*) Sketch to show flow induced by bridges which causes vortex stretching of threads, and flow induced by threads which causes vortex stretching of bridges. (*b*) Enstrophy production terms at $t = 6.0$ in π_d. Contour levels (min., max.) with constant increment are: Case A: Term I (−11.39, 24.98), Term II (−0.051, 0.469), Term III (−0.06, 0.056), Term IV (−18.87, 3.57), Case E: Term I (−2.27, 45.96), Term II (−0.12, 6.84), Term III (−0.448, 0.986), Term IV (−36.6, 4.9). (*c–e*) Vortex lines and isovorticity surfaces in the quadrant simulated, see figure 1(*b*). (*c*) Vortex lines starting at $|\omega|=9.0$ in π_s and π_d, and isovorticity surfaces for case A at $t=4.5$. (*d*) Vortex lines starting at $|\omega|=4.0$ in π_s and π_d, and isovorticity surfaces for case A at $t=6.0$. (*e*) Vortex lines starting at $|\omega|=6.0$ in π_s and π_d, and isovorticity surfaces for case E at $t=6.0$.

hold in general, especially for flows with multiple regions of strong dilatation, which would lead to significant changes in temperature and corresponding changes in fluid properties.

5.5. *Evolution of spectra*

In order to study the influence of compressibility at different lengthscales, we consider spectra of $\boldsymbol{u}$, P and ρ. We use Helmholtz decomposition of $\boldsymbol{u} = \boldsymbol{u}^C + \boldsymbol{u}^I$, with $\boldsymbol{u}^C$ such that $\nabla \times \boldsymbol{u}^C = 0$, $\nabla \cdot \boldsymbol{u}^C = \nabla \cdot \boldsymbol{u}$, and $\boldsymbol{u}^I$ such that $\nabla \times \boldsymbol{u}^I = \nabla \times \boldsymbol{u}$, $\nabla \cdot \boldsymbol{u}^I = 0$. The energy spectra associated with $\boldsymbol{u}^C$, $\boldsymbol{u}^I$, and $\boldsymbol{u}$ are shown in figure 18(*a*). In the low-M case A at $t = 0.5$, we note that $\boldsymbol{u}^C$ has much less energy than $\boldsymbol{u}^I$ except at high wavenumbers ($k = 30$). The high energy in $\boldsymbol{u}^C$ at these wavenumbers is likely to be due to acoustic waves, since no shocklet is present and we also see corresponding peaks in the spectra of P and ρ shown in figure 18(*b*) at this time. Note that the energy associated with these acoustic waves is very small (of order 10^{-7}). Thus, we can neglect the wave–vortex interactions as acoustic waves move across the adjacent domains due to periodic boundary conditions. At much later times ($t = 4.5$), most of the energy is associated with $\boldsymbol{u}^I$ at all wavenumbers, and between wavenumbers 5 and 13 we see a -5/3 slope; however, we cannot make conclusive statements about the presence of an inertial range owing to the relatively few modes present. In case E at $t = 0.5$, we find that energy in $\boldsymbol{u}^C$ is higher at all wavenumbers beyond 10. This is expected owing to the presence of a shocklet. At late times ($t = 4.5$), in case E the drop in kinetic energy is everywhere faster than $k^{-5/3}$, which suggests a higher energy dissipation compared to case A. This may be due to the additional dissipation involving dilatational velocity, which is particularly important when the shocklet is present (Lee *et al.* 1991). Also, the small-scale energy is higher at $t = 4.5$ than at $t = 0.5$, thereby indicating that vortex reconnection is in fact a cascade mechanism. The *Re* for the present simulations, however, is too low for comments to be made on the exponent of the energy spectrum at high M.

6. Concluding remarks

Vortex reconnection, a typical example of coherent structure interactions, is found to be significantly affected by compressibility. In particular, shocklet formation and the associated baroclinic vorticity production initiate reconnection (circulation transfer) at an early time, thereby altering the dynamics during the 'inviscid advection phase'. Even though the circulation transfer at late times is predominantly due to viscous cross-diffusion for all M, the higher Γ_d at early times which increases with M has a strong effect on the late-time dynamics. The rate of circulation transfer and peak vorticity are reduced at late times owing to stronger bridges at early times. This suggests that reconnection occurs over a longer timescale than in the incompressible case and that any possible finite-time singularity of vorticity (in π_s) for the incompressible Navier–Stokes equations in the limit of infinite Reynolds number may be suppressed by compressibility effects.

Compressibility effects also reduce the twisting of vortex lines in bridges at late times. Twisting of vortex lines is closely related to polarization of vortical structures. Polarization is inferred by applying the helical wave decomposition (HWD), which decomposes a vector field (e.g. vorticity) into two parts based upon the eigenfunctions of the curl operator (Melander & Hussain 1993). Each of these parts has an axial flow associated with it; for instance, for a rectilinear vortex column, the right-handed part has axial vorticity (half the magnitude of the rectilinear

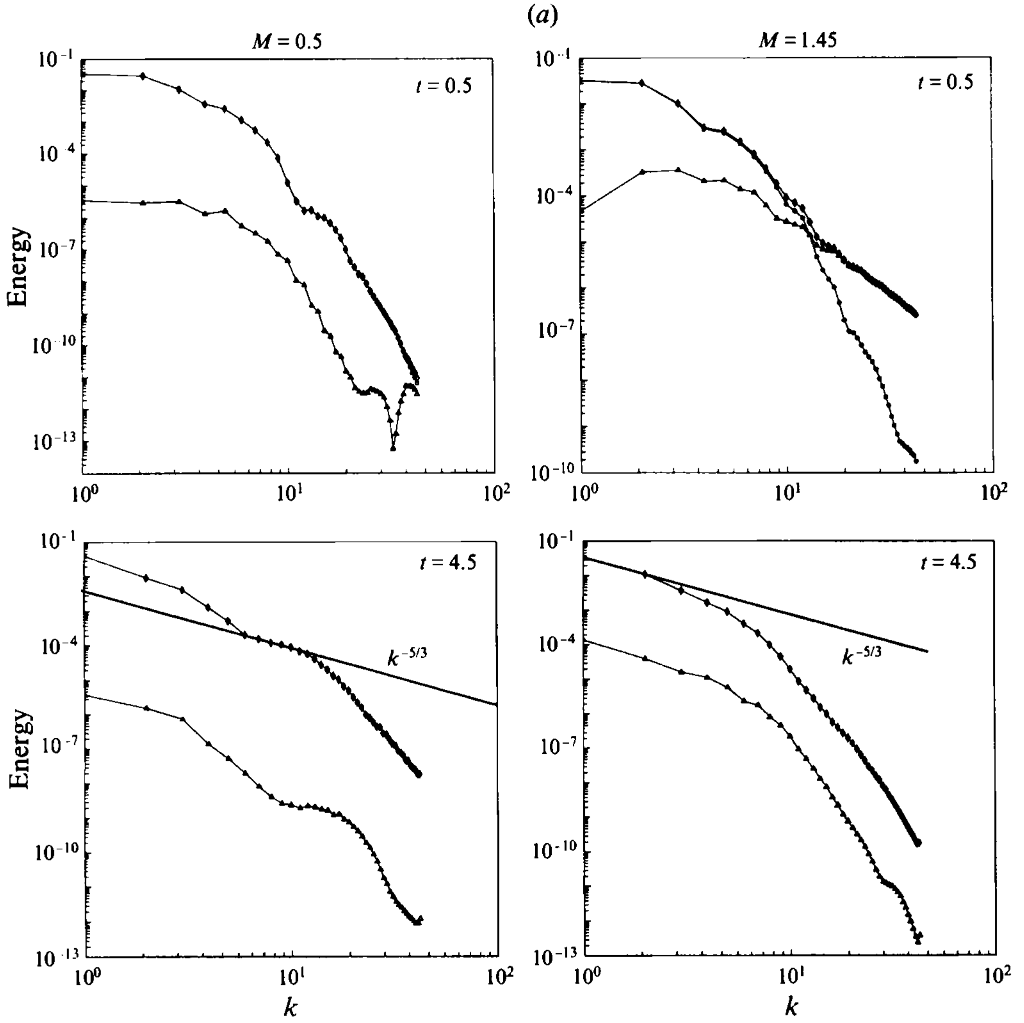

FIGURE 18 (*a*). For caption see facing page.

vortex) and axial flow in the same directions, while the left-handed part has axial vorticity (half the magnitude of the rectilinear vortex) and axial flow in the opposite directions – clearly, when these two polarized parts are superposed we obtain the original vortex with no axial flow. An alternative analysis of vortex reconnection based upon HWD is the subject of a separate study by us. Additionally, if the initial vortex tubes are polarized, i.e. dominated by one component with non-zero axial flow, the evolutionary dynamics can be significantly different, as illustrated by Virk *et al.* (1994) for axisymmetric vortex rings. Such an axial flow is likely to occur in contrails of aircraft. Further, Melander & Hussain (1993) observe that organized turbulent structures are typically polarized. This suggests that reconnection of polarized vortex tubes may be more relevant to turbulence dynamics.

An important issue common to both incompressible and compressible flows, which is beyond the scope of present work, is a precise definition of vortex reconnection. Such a definition is essential in order to assess the importance of reconnection in

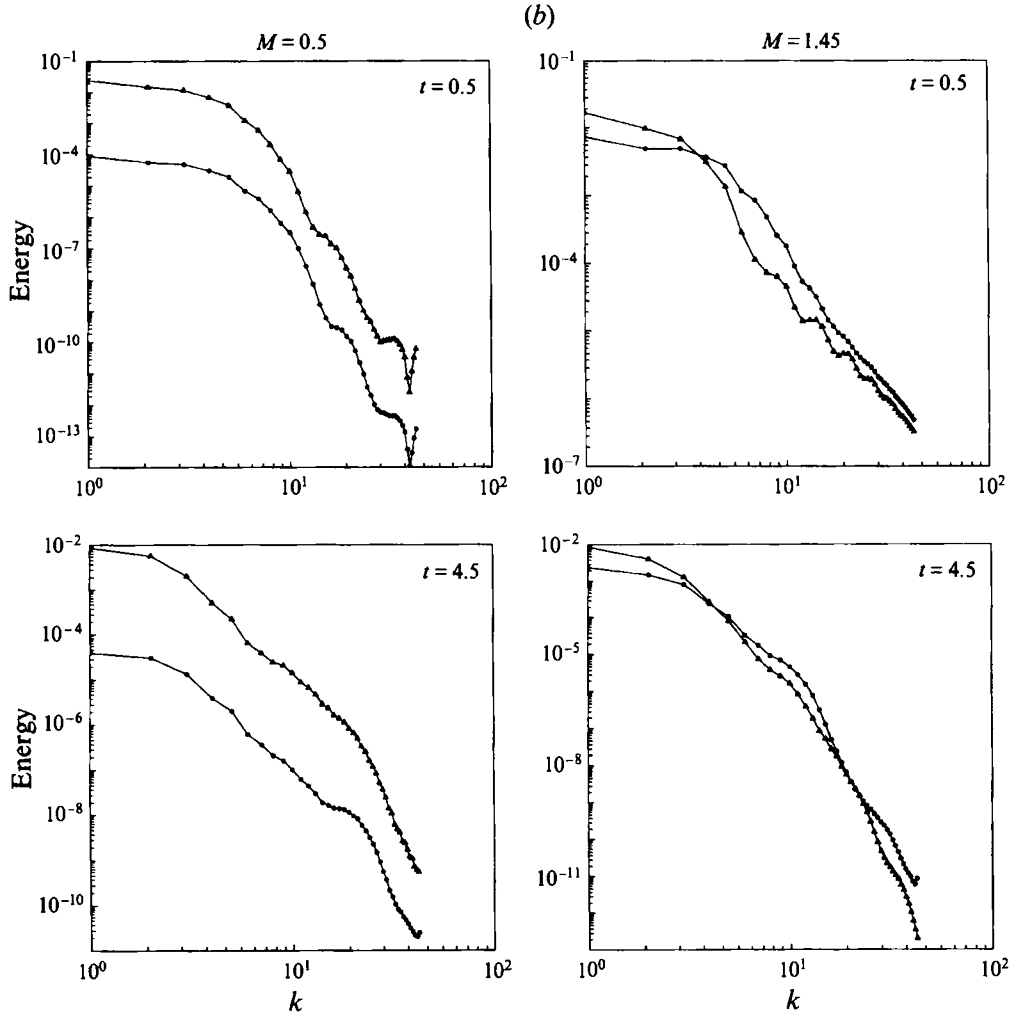

FIGURE 18. (*a*) Velocity spectra: Δ, compressible velocity u^c; ○, solenoidal velocity u^I; ◇, total u. The spectra for u^I and u are indistinguishable when $u^c \ll u^I$. (*b*) Spectra of P (Δ) and ρ (○).

turbulent flows. In general, the evolution of isovorticity surfaces is not an adequate diagnostic to determine vortex reconnection; this was clearly illustrated by Virk *et al.* (1994) for incompressible, axisymmetric flows with swirl. A definition of vortex reconnection has been suggested by Melander & Hussain (1994*a*) in axisymmetric flows with swirl by using a local analysis analogous to that used for magnetic reconnection studies (Greene 1988). In Greene's approach, a flux-preserving velocity $\hat{v}$ is defined to track vortex lines in a viscous flow. Reconnection occurs at the locations where $\hat{v}$ is singular, such as at vorticity nulls or on a closed vortex line. Generalization of this approach into a method for identifying reconnection in fully three-dimensional flows is, however, still lacking.

Kida & Takaoka (1991, 1994) have suggested a definition of the degree of reconnection as the magnitude of the term $R = \nu(\nabla^2\omega)_\perp$, which is the component of the viscous term in the incompressible vorticity equation perpendicular to the local vorticity vector. Since $\omega = 0$ along the X-axis, $(\nabla^2\omega)_\perp$ is undefined on this axis.

Nevertheless, in π_s and π_d, ω is non-zero, but R is still identically zero (inferred from inherent symmetries in the problem). Thus, this definition fails to show the reconnection occurring there. In addition, these authors provide an example (twisted vortex layer) where the topology of the vortex lines does not change at all, although R is non-zero, so that reconnection is incorrectly predicted by this definition. Further, being a point variable, R does not reflect the degree of reconnection. Finally, it is a subjective measure since the threshold value of R which indicates the occurrence of reconnection is unknown *a priori*. Hence the relevance of this approach to reconnection remains unclear.

The reason for the convective timescale of reconnection, a necessarily viscous interaction, requires further investigation. *Ad hoc* timescale definitions, based on the time for a reconnected line to move away from the interaction region (Saffman 1990) or the distance between the peak vorticity locations of interacting cores (Boratav *et al.* 1992), are not meaningful in a general situation. For instance, both these definitions fail in the reconnection of antiparallel vortex tubes. We did not see any sharp drops in the distance between peak vorticity locations, which Boratav *et al.* have used to define a reconnection timescale. Also, the reconnected vortex lines continuously move away from the interaction region; note that implicit in this statement is the ability to track vortex lines in a viscous flow – as mentioned above, reconnection occurs precisely when this is not possible (Greene 1988)!

Another aspect of the reconnection timescale which remains unresolved is its limit as $Re \rightarrow \infty$ and/or $M \rightarrow \infty$. Our results clearly show that the reconnection timescale defined as the time to reach $\Gamma_s = 0.5\Gamma_s(t = 0)$ increases with M; but we cannot simulate a higher M with the present initial conditions since P and ρ become negative in the core. Based on Saffman's model, Shelley *et al.* (1993) show analytically that this timescale in the incompressible case should *increase* as $\ln(Re)$; however, their simulations in a limited range of Re first show a decrease and then a much slower increase in the timescale. They suggest that inadequate modelling of strain rates may be responsible for this discrepancy. Melander & Hussain (1990) have proposed to define the reconnection timescale as the time to reach the first local maximum of $\mathrm{d}\Gamma_s/\mathrm{d}t$. This definition is based on the conceptual scenario that vortex reconnection occurs in bursts; at low Re (as in DNS), most Γ_s is transferred in one burst. But as $Re \rightarrow \infty$, the Γ_s transfer in each burst is infinitesimal. Based on a study of core dynamics, Melander & Hussain (1994*b*) predict that the duration of each burst reaches a finite limit, and this reconnection time decreases with increasing Re. Thus, we find that many fundamental issues regarding vortex reconnection remain controversial.

The present study clearly demonstrates that compressibility can significantly alter vorticity dynamics, especially during reconnection. Therefore, additional studies of idealized vorticity configurations are needed to develop a better understanding of coherent structure interactions in compressible turbulent flows to permit their modelling and control.

The authors are grateful to M. V. Melander for many insightful discussions and to W. Schoppa for a careful review of the manuscript. This research is supported by NSF grant CTS-9214818. During an early part of this project, D.V. was supported by the Advanced Study Program of NCAR, Boulder. Some of the simulations and analyses reported here were carried out on the NAS facility at NASA Ames Research Center under grant no. RNS:258-6/629/5712.

REFERENCES

ASHURST, W. T. & MEIRON, D. I. 1987 Numerical study of vortex reconnection. *Phys. Rev. Lett.* **58**, 1632–1635.

BAIRD, J. P. 1987 Supersonic vortex rings. *Proc. R. Soc. Lond.* A, **409**, 59–65.

BORATAV, O. N., PELZ, R. B. & ZABUSKY, N. J. 1992 Reconnection in orthogonally interacting vortex tubes: Direct numerical simulations and quantifications. *Phys. Fluids* A **4**, 581–605.

BRIDGES, J., HUSAIN, H. S. & HUSSAIN, F. 1989 Whither coherent structures? In *Whither Turbulence? Turbulence at the Crossroads* (ed. J. L. Lumley), 132–150. Springer.

BROADBENT, E. G. & MOORE, D. W. 1987 The interaction of a vortex ring and a coaxial supersonic jet. *Proc. R. Soc. Lond.* A **409**, 47–57.

BUNTINE, J. D. & PULLIN, D. I. 1989 Merger and cancellation of strained vortices. *J. Fluid Mech.* **205**, 263–295.

CROW, S. C. 1970 Stability theory for a pair of trailing vortices. *AIAA J.* **8**, 2172–2179.

ERLEBACHER, G., HUSSAINI, M. Y., KREISS, H. & SARKAR, S. 1990 The analysis and simulation of compressible turbulence. *ICASE Rep.* 90–15.

FEIEREISEN, W. J., REYNOLDS, W. C. & FERZIGER, J. H. 1981 Numerical simulation of a compressible, homogeneous, turbulent shear flow. *Rep. TF-13.* Stanford University.

FOHL, T. & TURNER, J. S. 1975 Colliding vortex rings. *Phys. Fluids* **18**, 433–436.

GREENE, J. M. 1988 Geometrical properties of three-dimensional reconnecting magnetic fields with nulls. *J. Geophys. Res.* **93**, 8583–8590.

HEISTER, S. D., MCDONOUGH, J. M., KARAGOZIAN, A. R. & JENKINS, D. W. 1990 The compressible vortex pair. *J. Fluid Mech.* **220**, 339–354.

HOWARD, L. N. & MATTHEWS, D. L. 1956 On the vortices produced in shock diffraction. *J. Appl. Phys.* **26**, 223–231.

HUSSAIN, F. 1986 Coherent structures and turbulence. *J. Fluid Mech.* **173**, 303–356.

HUSSAIN, F. & HUSAIN, H. S. 1989 Elliptic jets. Part 1. Characteristics of unexcited and excited jets. *J. Fluid Mech.* **208**, 257–320.

KAMBE, T. 1983 A class of exact solutions of two-dimensional viscous flow. *J. Phys. Soc. Japan* **52**, 834–841.

KERR, R. & HUSSAIN, F. 1989 Simulation of vortex reconnection. *Physica* D **37**, 474–484.

KIDA, S. & TAKAOKA, M. 1987 Bridging in vortex reconnection. *Phys. Fluids* **30**, 2911–2914.

KIDA, S. & TAKAOKA, M. 1991 Breakdown of frozen motion of vorticity field and vortex reconnection. *J. Phys. Soc. Japan* **60**, 2184–2196.

KIDA, S. & TAKAOKA, M. 1994 Vortex reconnection. *Ann. Rev. Fluid Mech.* **60**, 169–189.

KIDA, S., TAKAOKA, M. & HUSSAIN, F. 1989 Reconnection of two vortex rings. *Phys. Fluids* A **1**, 630–632.

KIDA, S., TAKAOKA, M. & HUSSAIN, F. 1991*a* Collision of two vortex rings. *J. Fluid Mech.* **230**, 583–646.

KIDA, S., TAKAOKA, M. & HUSSAIN, F. 1991*b* Formation of head-tail structure in two-dimensional straining flow. *Phys. Fluids* A **3**, 2688–2697.

LEE, S., LELE, S. K. & MOIN, P. 1991 Eddy shocklets in decaying compressible turbulence. *Phys. Fluids* A **3**, 657–664.

LIM, T. T. 1989 An experimental study of a vortex ring interacting with an inclined wall. *Exps. Fluids* **7**, 453–463.

MANDELLA, M. J. 1987 Experimental and analytical studies of compressible vortices. PhD thesis, Stanford University.

MEIRON, D. I., SHELLEY, M. J., ASHURST, W. T. & ORSZAG, S. A. 1989 Numerical studies of vortex reconnection. In *Mathematical Aspects of Vortex Dynamics* (ed. R. Caflisch). SIAM.

MELANDER, M. V. & HUSSAIN, F. 1988 Cut-and-connect of two antiparallel vortex tubes. *CTR Rep. S-88*, pp. 257-286 (referred to herein as MH 1988).

MELANDER, M. V. & HUSSAIN, F. 1989 Cross-linking of two antiparallel vortex tubes. *Phys. Fluids* A **1**, 633–636.

MELANDER, M. V. & HUSSAIN, F. 1990 Topological aspects of vortex reconnection. In *Topological Fluid Mechanics* (ed. H.K. Moffatt & A. Tsinober), pp. 485–499. Cambridge University Press.

MELANDER, M. V. & HUSSAIN, F. 1993 Coupling between a coherent structure and fine-scale turbulence. *Phys. Rev.* E **48**, 2669–2689.

Melander, M. V. & Hussain, F. 1994*a* Topological vortex dynamics in axisymmetric viscous flows. *J. Fluid Mech.* **260**, 57–80.

Melander, M. V. & Hussain, F. 1994*b* Core dynamics on a vortex column. *Fluid Dyn. Res.* **13**, 1–37.

Meng, H. & Hussain, F. 1995 Instantaneous flow field in an unstable vortex ring measured by holographic particle velocimetry. *Phys. Fluids* **7**, 9–11.

Moore, D. W. & Pullin, D. I. 1987 The compressible vortex pair. *J. Fluid Mech.* **185**, 171–204.

Moser, R. D. & Rogers, M. M. 1993 The three-dimensional evolution of a plane mixing layer: pairing and transition to turbulence. *J. Fluid Mech.* **247**, 275–320.

Oshima, Y. & Izutzu, N. 1988 Cross-linking of two vortex rings. *Phys. Fluids* **31**, 2401.

Passot, T. & Pouquet, A. 1987 Numerical simulation of compressible homogeneous flows in the turbulent regime. *J. Fluid Mech.* **181**, 441–466.

Pumir, A. & Siggia, E. 1990 Collapsing solutions to the three-dimensional Euler equations. *Phys. Fluids* A **2**, 220–241.

Saffman, P. 1990 A model of vortex reconnection. *J. Fluid Mech.* **212**, 395–402.

Schatzle, P. 1987 An experimental study of fusion of vortex rings. PhD thesis, California Institute of Technology.

Schoppa, W., Hussain, F. & Metcalfe, R. 1995 A new mechanism of small-scale transition in a plane mixing layer: core dynamics of spanwise vortices. *J. Fluid Mech.* **298**, 23–80

Shelley, M. J., Meiron, D. I. & Orszag, S. A. 1993 Dynamical aspects of vortex reconnection of perturbed anti-parallel vortex tubes. *J. Fluid Mech.* **246**, 613–652.

Siggia, E. 1985 Collapse and amplification of a vortex filament. *Phys. Fluids* **28**, 794–805.

Takaki, R. & Hussain, F. 1985 Recombination of vortex filaments and its role in aerodynamic noise. In *Proc. 5th Symp. on Turbulent Shear Flows*, pp. 3.19–3.25. Cornell University.

Thompson, P. A. 1984 *Compressible-Fluid Dynamics*. McGraw-Hill.

Virk, D. 1993 Numerical studies of vortex dynamics: compressible reconnection and a polarized ring. PhD thesis, University of Houston.

Virk, D. & Hussain, F. 1993 Influence of initial conditions on compressible vorticity dynamics. *Theor. Comput. Fluid Dyn.* **5**, 309–334.

Virk, D., Melander, M. V. & Hussain, F. 1994 Dynamics of a polarized vortex ring. *J. Fluid Mech.* **260**, 23–55.

Wray, A. A. 1987 Very low storage time-advancement schemes. *Internal Report*. NASA Ames Research Center, Moffett Field, California.

Zabusky, N. J. & Melander, M. V. 1989 Three-dimensional vortex tube reconnection: morphology for orthogonally-offset tubes. *Physica* D **37**, 555–562.

Zank, G. P. & Matthaeus, W. H. 1991 The equations of nearly incompressible fluids. I. Hydrodynamics, turbulence, and waves. *Phys. Fluids* A **3**, 69–82.